



**HAL**  
open science

## Enhanced photocatalytic activity of hydrozincite-TiO<sub>2</sub> nanocomposite by copper for removal of pharmaceutical pollutant mefenamic acid in aqueous solution

Lekbira El Mersly, El Mountassir El Mouchtari, El Mostafa Moujahid, Samir Briche, Abdelaaziz Alaoui Tahiri, Claude Forano, Vanessa Prévot, Salah Rafqah

### ► To cite this version:

Lekbira El Mersly, El Mountassir El Mouchtari, El Mostafa Moujahid, Samir Briche, Abdelaaziz Alaoui Tahiri, et al.. Enhanced photocatalytic activity of hydrozincite-TiO<sub>2</sub> nanocomposite by copper for removal of pharmaceutical pollutant mefenamic acid in aqueous solution. *Environmental Science and Pollution Research*, 2023, 30 (9), pp.24575-24589. 10.1007/s11356-022-23832-w . hal-03843091

**HAL Id: hal-03843091**

**<https://uca.hal.science/hal-03843091v1>**

Submitted on 7 Nov 2022

**HAL** is a multi-disciplinary open access archive for the deposit and dissemination of scientific research documents, whether they are published or not. The documents may come from teaching and research institutions in France or abroad, or from public or private research centers.

L'archive ouverte pluridisciplinaire **HAL**, est destinée au dépôt et à la diffusion de documents scientifiques de niveau recherche, publiés ou non, émanant des établissements d'enseignement et de recherche français ou étrangers, des laboratoires publics ou privés.

1           **Enhanced photocatalytic activity of Hydrozincite-TiO<sub>2</sub> nanocomposite by copper for removal of**  
2           **pharmaceutical pollutant mefenamic acid in aqueous solution**

3   Lekbira El Mersly<sup>1</sup>, El Mountassir El Mouchtari<sup>1</sup>, El Mostafa Moujahid<sup>2</sup>, Samir Briche<sup>3</sup>, Abdelaaziz Alaoui Tahiri<sup>1</sup>,  
4           Claude Forano<sup>4</sup>, Vanessa Prevot<sup>4</sup> and Salah Rafqah<sup>1\*</sup>

5  
6   <sup>1</sup> Laboratoire de Chimie Analytique et Moléculaire, Faculté Polydisciplinaire de Safi, Université Cadi Ayyad,  
7   Morocco.

8   <sup>2</sup> Laboratoire Physico-Chimie des Matériaux, Faculté des Sciences, Université Chouaib Doukkali, EL Jadida,  
9   Morocco

10   <sup>3</sup> Département Stockage de l'Energie et Revêtements Multifonctionnels (SERM), MAScIR Foundation, Rabat,  
11   Morocco.

12   <sup>4</sup> Université Clermont Auvergne, Clermont Auvergne INP, CNRS, ICCF, F-63000 Clermont-Ferrand, France.

13  
14   \* Corresponding author: Pr. Salah RAFQAH (E-mail: [rafqah@gmail.com](mailto:rafqah@gmail.com))

15   Laboratoire de Chimie Analytique et Moléculaire (LCAM)

16   Département de Chimie, Faculté Polydisciplinaire de Safi

17   Université Cadi Ayyad.

18   Sidi Bouzid, B.P. 4162, 46000 Safi Maroc

19   Tel : 00-212-524669357 ;Fax : 00-212-524669516.

30 **Abstract**

31 Nanocomposites based on Hydrozincite-TiO<sub>2</sub> and copper-doped HZ-xCu-TiO<sub>2</sub> (x= 0.1; 0.25; 0.35) were synthesized  
32 in a single step using the urea method. The samples were characterized by XRD, FTIR, SEM/TEM and DRS. The  
33 study of adsorption capacity and photocatalytic efficiency of these nanocomposites have been tested on a  
34 pharmaceutical pollutant, mefenamic acid (MFA).

35 Kinetic study of removal of MFA, indicates that this pollutant was adsorbed on the surface of the synthesized  
36 phases, according to Langmuir's model. Such adsorption proved to be well adapted in a kinetic pseudo-second order  
37 model with capacity of 13.08 mg/g for HZ-0.25Cu-TiO<sub>2</sub>. Subsequently, the kinetics of photocatalytic degradation  
38 under UV-visible irradiation was studied according to several parameters, which allowed us to optimize our  
39 experimental conditions.

40 The nanocomposite HZ-0.25Cu-TiO<sub>2</sub> showed significant removal efficiency of MFA. Elimination rate reached  
41 100% after 20 min under UV-vis irradiation, and 77% after 7h under visible light irradiation. Repeatability tests  
42 have shown that this nanocomposite is extremely stable after six photocatalytic cycles. By-products of MFA were  
43 detected by LC/MS. These photoproducts produced by three types of reactions of hydroxylation; cyclization and  
44 cleavage of the aromatic ring. MFA underwent complete mineralization after 22 h of irradiation in the presence of  
45 the HZ-0.25Cu-TiO<sub>2</sub>.

46

47 **Keywords:** Hydrozincite-TiO<sub>2</sub>, Layered Simple Hydroxide (LSH), Copper, nanocomposite, Photocatalysis,  
48 Mefenamic Acid.

49

50 **1. Introduction**

51 Many pharmaceutical compounds for medical and veterinary uses are release, at least in part, through wastewater  
52 treatment plants into natural waters. Indeed, wastewater contains new organic substances, such as anti-inflammatory  
53 drugs, which are non-biodegradable and consequently not effectively removed by conventional wastewater  
54 treatment processes (Ternes et al. 2002; Li and Jin 2009). As a result, these pharmaceuticals end up as persistent  
55 contaminants in water bodies even in trace amounts (from ng/L to µg/L) and could cause dramatic impact on human  
56 health and/or biodiversity (Sim et al. 2010; Sui et al. 2015; El Mouchtari et al. 2020).

57 As an example, 2-(2,3-dimethyl phenyl) aminobenzoic acid, named as Mefenamic acid (MFA), is an anti-  
58 inflammatory agent used in an extended way for the treatment of several pathologies such as osteoarthritis,  
59 nonarticular rheumatism, sports injuries, and other painful musculoskeletal illnesses (Mucklow 2000;  
60 Abdolmohammad-Zadeh et al. 2014). Overdose of mefenamic acid produces toxic metabolite accumulation that  
61 causes nausea, vomiting, and sometimes diarrhea (Mucklow 2000; Abdolmohammad-Zadeh et al. 2014). Many  
62 studies have indicated that conventional sewage treatment plants cannot effectively remove MFA, which has been  
63 detected in wastewater effluents as well as in receiving waters in different countries (Soulet et al. 2002; Tauxe-  
64 Wuersch et al. 2005; Jones et al. 2006; Gros et al. 2007; Araujo et al. 2011; Colombo et al. 2016). Fen et al. (Fent et  
65 al. 2006) showed that MFA was detected at concentrations around 0.43  $\mu\text{g/L}$  in several environmental  
66 compartments.

67 To overcome the release of pharmaceuticals into environmental compartments, various treatment techniques and  
68 processes have been used. Over the last few decades, photodegradation has been frequently promoted as an effective  
69 strategy to reduce the recalcitrant pharmaceutical pollutants (PPs) (Chen et al. 2015, 2016a) from wastewaters and to  
70 minimize the release of toxic products that could endanger natural ecosystems. In this context, light-activated  
71 advanced oxidation processes (AOP) using heterogeneous photocatalysts with enhanced pollutant adsorption  
72 properties are the subject of extensive investigation. Obviously, adsorption coupled with photodegradation leads to a  
73 significant efficiency on the treatment of several pollutants (Tijani et al. 2014).

74 Several studies have reported the photocatalytic elimination of MFA in aqueous solution using photocatalyst-based  
75 composite materials. Shirzadi et al. evaluated the photocatalytic activity of mixed metal oxide ZnO–CuO system,  
76 supported onto clinoptilolite nanoparticles (NCP), treated by ball milling, for the photodegradation of MFA in  
77 aqueous solution under UV-C radiation (Shirzadi and Nezamzadeh-Ejehieh 2016).  $\text{CuO}_{6.9\%}\text{-ZnO}_{5.3\%}/\text{NCP}$  catalyst  
78 display the best photodegradation activity compared to bulk or supported CuO or ZnO oxide.

79 Olga Gimeno et al. (Gimeno et al. 2010) found that the elimination of MFA by a combined process of adsorption on  
80 activated carbon and UV irradiation plus ozonation oxidation, reached 60% mineralization after 120 min. Manali  
81 Rathod et al. (Rathod et al. 2018) studied the degradation process of MFA in aqueous solution under UV radiation in  
82 presence of nanocellulose-supported  $\text{TiO}_2$  nanoparticles. Several mass fractions were prepared by an ultrasonic  
83 impregnation method, while the 10%  $\text{TiO}_2$  loading in nanocellulose showed the best photocatalytic efficiency and  
84 reusability even after five cycles of degradation.

85 Hydrozincite ( $\text{Zn}_5(\text{CO}_3)_2(\text{OH})_6$ ), one of the members of the layered simple hydroxides (LSH) family, appears as an  
86 interesting material for such combined process. Liu et al. (Liu and Teng 2018a) reported that  $\text{Zn}_5(\text{CO}_3)_2(\text{OH})_6$   
87 display greater photoactivity toward methylene blue than  $\text{ZnCO}_3$ , due to the larger band gap of hydrozincite (5.04

88 eV) that increases the oxidation potential of valence band. Hydrozincite has been widely employed as a precursor of  
89 photoactive ZnO semiconductor used, for example, for the H<sub>2</sub> production (Yan and Xue 2006a; Jaramillo-Páez et al.  
90 2017). Moreover, thanks to its 2D structure, Zn<sub>5</sub>(CO<sub>3</sub>)<sub>2</sub>(OH)<sub>6</sub> may display high specific surface area for pollutant  
91 adsorption, which could combine favorably with photoactive properties. However, hydrozincite has not yet been  
92 fully investigated, although it is very abundant in nature, non-toxic and can be produced at low cost. To the best of  
93 our knowledge, very little work has been devoted to evaluate the photocatalytic properties of hydrozincite. Papers  
94 that reported the photodegradation of dye molecules (Liu and Teng 2018a) or phenolic compounds  
95 (Tzompantzi- Flores et al. 2019) by Zn<sub>5</sub>(CO<sub>3</sub>)<sub>2</sub>(OH)<sub>6</sub> show that a long irradiation time was required, i.e. several  
96 hours under UV-light irradiation. On the other hand, Hydrozincite has not yet been evaluated for the elimination of  
97 pharmaceuticals pollutants in aqueous medium.

98 A strategy that is now attracting a great attention is the design of heterojunction structures combining two or more  
99 semiconductors (metal oxides or metal sulphides) or doped metal oxides (Cherepanova et al. 2017a;  
100 Tzompantzi- Flores et al. 2019), which allows minimizing the charge carrier(e<sup>-</sup>, h<sup>+</sup>) recombination and also tuning  
101 the valence band and conducting band potentials in order to develop efficient visible light photocatalysts.

102 The copper-doped hydrozincite could provide a wide surface area for electron transfer while the titanium dioxide  
103 reduces the recombination through the generated holes attraction. The photocatalytic performance of these  
104 heterojunctions arises from a synergic effect between TiO<sub>2</sub> and hydrozincite sheets.

105 Indeed, the objective of this work is the study of the photodegradation of the bio-recalcitrant pharmaceutical  
106 pollutant mefenamic acid (MFA) by using a novel nanocomposite material based on TiO<sub>2</sub> and copper-doped  
107 synthetic hydrozincite. The novelty lies in the improvement of the photocatalytic efficiency by the combination of  
108 adsorption capacity and photocatalytic in order to obtain a nanocomposite with high photocatalytic activity. The  
109 nanocomposite materials were prepared by the combination of one-step coprecipitation and hydrothermal process.  
110 The as-obtained materials were tested in the photodegradation of compounds that are too difficult to eliminate such  
111 as the mefenamic acid molecule. The Cu-doping carried out in this study leads us to believe that use in  
112 photocatalytic applications under sunlight irradiation could be of considerable interest. These materials have also  
113 shown significant recyclability and total mineralization of the pollutant and its photoproducts in the aqueous  
114 solution.

## 115 **2. Material and Methods**

### 116 **2.1. Chemicals**

117 All chemicals were of analytical quality and were used without any purification. Copper (II) chloride (CuCl<sub>2</sub>),  
118 perchloric acid (HClO<sub>4</sub>), and sodium hydroxide (NaOH) were purchased from Loba Chemie, and mefenamic acid

119 (MFA) was purchased from Acros Organics. Zinc (II) chloride ( $\text{ZnCl}_2$ ), titanium tetrachloride ( $\text{TiCl}_4$ ), urea  
120 ( $\text{CH}_4 \text{N}_2 \text{O}$ ), acetonitrile (HPLC grade) were supplied by Sigma Aldrich and hydrochloric acid (HCl) was from  
121 prolabo/VWR.

122 The aqueous solution of MFA was prepared at a concentration of  $5.0 \times 10^{-5} \text{mol.L}^{-1}$  with ultrapure water from a  
123 Millipore device (Direct-Q® 5 UV) after 24 hours of stirring at room temperature ( $25^\circ\text{C}$ ) under dark.

## 124 2.2. Synthesis procedure

125  $\text{Zn}_5(\text{CO}_3)_2(\text{OH})/\text{TiO}_2$  (HZ- $\text{TiO}_2$ ) nanocomposite was prepared via a fast coprecipitation of zinc and titanium salts in  
126 presence of the urea.  $\text{TiCl}_4$  (0.44 ml),  $\text{ZnCl}_2$  (2.38 g) and urea (6.0 g) were dissolved in deionized water (200 ml)  
127 under vigorous stirring for 30 min. The resulting solution was introduced into the autoclave for treatment at  $130^\circ\text{C}$   
128 for 48h under autogenous pressure (Shao et al. 2011). The solid product was recovered by centrifugation and then  
129 washed several times. Finally, the solid product was dried at  $60^\circ\text{C}$  for 12h.

130 To evaluate the effect of  $\text{Cu}^{2+}$  on the photocatalytic properties of HZ- $\text{TiO}_2$  nanocomposite, a series of Cu doped  
131 synthetic hydrozincite samples were prepared using the same procedure as described before, by varying the Zn:Cu  
132 molar ratio (90:10, 75:25 and 65:35). For all synthesis, the ratio  $(\text{Cu}^{2+} + \text{Zn}^{2+})/\text{Ti}^{4+}$  was kept constant at 2:1. The  
133 nanocomposite samples were labeled as HZ-xCu- $\text{TiO}_2$ , where x is the molar ratio of Cu.

## 134 2.3. Material characterizations

135 X-ray diffraction (XRD) measurements were recorded on a Philips Pro powder diffractometer using the Cu X-ray  
136 source  $\text{K}_\alpha$  ( $\lambda = 1.5405 \text{ \AA}$ ) as the incident radiation. The diffractograms were recorded between  $5^\circ$ - $70^\circ$  in 2 theta at an  
137 accelerating voltage of 40 kV, a filament current of 30 mA and a scanning speed of  $2^\circ \cdot \text{min}^{-1}$ . The FTIR spectra of  
138 the different samples were recorded with a Thermo Scientific IR spectrophotometer over a range of  $400$ - $4000 \text{ cm}^{-1}$ ,  
139 using KBr pellets for sample preparation. The morphology and structure of the sample were observed by high-  
140 resolution scanning electron microscopy (HR-SEM) using the BRUKER-QUANTAX FEI instrument operating at  
141 200 keV. The UV-vis diffuse reflectance and absorbance spectra were recorded by a Shimadzu UV-2600  
142 spectrometer equipped with an integrating sphere using  $\text{BaSO}_4$  as a reference and Raman spectroscopy (Confotec  
143 MR520) with laser of wavelength ( $\lambda = 532 \text{ nm}$ )

## 144 2.4. Adsorption experiments

145 Kinetics of adsorptions were performed by contacting a suspension of materials ( $0.4 \text{ g.L}^{-1}$ ) with a MFA solution at a  
146 concentration of  $5.0 \times 10^{-5} \text{mol.L}^{-1}$ , in the dark, at  $20^\circ\text{C}$ , under stirring. The concentration of residual MFA was  
147 determined by LC analysis for liquid samples withdrawn at different time steps. The amount of MFA adsorbed at a

148 contact time  $t$  ( $Q_t$ ) was plotted versus the residual MFA concentration in solution at  $t$  ( $C_t$ ).  $Q_t$  ( $\text{mg.g}^{-1}$ ) was calculated  
149 using eq.1:

$$150 \quad Q_t = (C_i - C_t) \times \frac{V}{m} \quad (\text{eq.1})$$

151 where  $C_i$ ,  $C_t$ ,  $V$  and  $m$  are the initial concentration and the concentration at  $t$  ( $\text{mg.L}^{-1}$ ) of the pharmaceuticals, the  
152 volume of the solution (L), and the solid weights (g), respectively.

153 The adsorption experiments performed by contacting suspensions of materials ( $0.4 \text{ g.L}^{-1}$ ) with MFA at different  
154 initial concentrations  $C_i$  ( $C_i = 2; 5; 10; 12$  and  $20 \text{ mg.L}^{-1}$ ) in the dark, under stirring, at  $20^\circ\text{C}$  for 30min of  
155 equilibrium time. The concentration ( $Q_0$ ) of MFA adsorbed by solids at equilibrium was plotted versus the residual  
156 MFA concentration in solution  $C_e$  ( $1.02; 2.85; 6.8; 8.5; 14.8 \text{ mg.L}^{-1}$ ).  $Q_0$  ( $\text{mg.g}^{-1}$ ) was calculated using eq.2:

$$157 \quad Q_0 = (C_i - C_e) \times \frac{V}{m} \quad (\text{eq.2})$$

158 where  $C_i$ ,  $C_e$ ,  $V$  and  $m$  are the initial concentration and the concentration at equilibrium time ( $\text{mg.L}^{-1}$ ) of the  
159 pharmaceuticals, the volume of the solution (L), and the solid weights (g), respectively.

160 The adsorption isotherms were plotted as  $Q_e$  versus  $C_e$  and fitted using the two standards isotherm models, the  
161 Langmuir and Freundlich models.

162 The Langmuir model is based on the following assumptions: the formation of a single adsorbate layer on the surface  
163 of the adsorbent, the existence of defined adsorption sites with same adsorption energy, an uniform surface layer  
164 without any interaction between the adsorbed molecules (Pirillo et al. 2009; Ansari and Mosayebzadeh 2010; Sun et  
165 al. 2013). The linear form of the Langmuir equation is written as follows (eq.3) (Mittal et al. 2009):

$$166 \quad \frac{C_e}{Q_e} = \frac{C_e}{Q_m} + \frac{1}{Q_m K_L} \quad (\text{eq.3})$$

167 Where  $Q_m$  ( $\text{mg.g}^{-1}$ ) is the maximum adsorption capacity, and  $K_L$  is an isothermal constant of the Langmuir model.  
168  $Q_m$  and  $K_L$  are determined from the curve between  $C_e/Q_e$  and  $C_e$ .

169 The Freundlich model is based on an equation that translates a variation in energy with the amount adsorbed. This  
170 variation in interaction energies is explained by the heterogeneity of the adsorption sites. Unlike the Langmuir  
171 model, the Freundlich equation does not provide an upper limit to adsorption, which limits its application to diluted  
172 media (Yagub et al. 2014). This model does, however, admit the existence of certain interactions between the  
173 adsorbed molecules. The linear form of the of Freundlich equation is (eq.4) (Freundlich 1906).

$$174 \quad \text{Log } Q_e = \text{Log } K_f + \frac{1}{n} \text{Log } C_e \quad (\text{eq.4})$$

175 Where  $K_f$  and  $n$  are the Freundlich constants, indicating the adsorption capacity and intensity, respectively.

176

## 177 2.5. Photocatalysis experiments

178 The irradiation tests were realized using a 300 W OsramUltra-Vitalux lamp equipped with a high-pressure tungsten  
179 filament. The intensity of incident UVA light (320-400 nm) is around 90 W.m<sup>-2</sup> and that of the visible range (400-  
180 700 nm) is 112 W.m<sup>-2</sup>. The tests with visible light were carried out with the same lamp using a UV filter (high-pass  
181 interference filter: 400FH90-50) absorbing all radiation below 400 nm. 50 mL of the mixture was placed in a  
182 double-jacketed glass reactor, which allowed maintaining the temperature at 20 °C of the solution during the  
183 irradiation time. Small solution aliquots (500 µl) were periodically withdrawn by using a syringe and filtered  
184 through a 0.2 µm Millipore filter to measure the variations of MFA concentration.

## 185 2.6. HPLC and TOC analysis

186 The concentration of the pharmaceuticals was determined by a liquid chromatography apparatus (UPLC Shimadzu)  
187 with a column C18 (5 µm; 4.6 × 150 mm). An isocratic method set at a flow rate of 1.0 ml.min<sup>-1</sup>. The injected  
188 volume was equal to 20 µL. The separation was obtained using a mixture of water (with 0.1% acetic  
189 acid)/acetonitrile in a ratio of 25:75 for the analysis. The detection of pharmaceuticals was performed using an  
190 absorption wavelength of 283 nm. Before injection, the samples were filtered through 0.2 µm filters of 25 mm  
191 diameter.

192 LC/MS studies were carried out with a Dionex Chromatography system coupled to a TSQ Endura™ Triple  
193 Quadrupole Mass Spectrometer equipped with a pneumatically assisted electrospray ionisation source (ESI). Total  
194 organic carbon (TOC) was analysed by direct injection of the collected samples into a Shimadzu TOC-L<sub>CPH/CPN</sub>  
195 analyser calibrated with standard solutions of hydrogen potassium phthalate.

## 196 2.7. Recycling and reuse test

197 To determine the reutilization of HZ-xCu-TiO<sub>2</sub> photocatalyst, recycling tests were carried out in the presence of 20  
198 mg of photocatalyst in the MFA aqueous solution of concentration  $5.0 \times 10^{-5} \text{ mol.L}^{-1}$ , after 20 minutes of irradiation.  
199 The photocatalyst was separated by simple filtration after each treatment. The filtrate was analysed by HPLC to  
200 determine the MFA concentration. The solid was recovered and dried at room temperature for 3 days, and re-  
201 dispersed again in a new MFA solution for further treatment. This procedure has been repeated 5 times and the  
202 removal rate after each cycle is calculated by the following equation:

$$203 \quad \% \text{ removal} = \frac{C_i - C_f}{C_i} \times 100 \quad (\text{eq.5})$$

204 Where C<sub>i</sub> and C<sub>f</sub> are the initial and final concentration of MFA.

## 205 3. Results and discussion

### 206 3.1. Structural characterization



### 207 3.1.1 Powder X-ray diffraction and FT-IR spectroscopy

208 The XRD analysis (**Figure 1a**) for all synthesized samples exhibit characteristic reflection peaks (200), (201), (310),  
209 (020), (311), (401), (510), (112), (330), (512), (-332) and (313), corresponding to the monoclinic hydrozincite,  
210  $Zn_5(CO_3)_2(OH)_6$  (JCPDS card N° 72-1100, space group C2/m) (Fig.1a). In addition, as shown in Fig. 1a, the  
211 diffractograms showed a second phase, attributed to the anatase  $TiO_2$  structure (JCPDS N° 84-1286), suggesting the  
212 formation of a HZ/ $TiO_2$  nanocomposite. We must noticed that these nanocomposites have, until now, often been  
213 considered as Zn-Ti layered double hydroxide with incorporation of  $Ti^{4+}$  in the brucitic sheets (Shao et al. 2011;  
214 Wang et al. 2017). However, Intissar et al. (Intissar et al. 2004) clearly shows by the X-ray absorption spectroscopy  
215 that the Ti cations do not penetrate into the Layered Double Hydroxide sheets but disperse on the sheets in the form  
216 of  $TiO_2$  anatase. Obviously, the diffraction lines of the HZ/ $TiO_2$  XRD patterns cannot be indexed using the  
217 hexagonal system with the rhomboedral symmetry (R-3m space group), as for LDH structures. On the other hand,  
218 while the synthesis conditions that we used may allow the doping of  $TiO_2$  by  $Zn^{2+}$  or  $Cu^{2+}$  cations (Yu et al. 2015;  
219 Mathew et al. 2018; Jiang et al. 2021), no evidence of such doping was inferred from XRD data. Then, our results  
220 demonstrate that the coprecipitation-hydrothermal process used for the synthesis of HZ/ $TiO_2$  promotes the formation  
221 of the  $TiO_2$  outside the hydrozincite structure. Beside, given the very close ionic radius of  $Zn^{2+}$  (0.74 Å) and  $Cu^{2+}$   
222 (0.72 Å), the incorporation of small amount of Cu in the synthetic hydrozincite may occur without inducing too  
223 much modification in the crystalline structure, thus leading to lattice parameters very close to those of natural  
224 hydrozincite (Ghose 1964), as shown in table 1 for the as-prepared samples  $(Zn_{1-x}Cu_x)_5(OH)_6(CO_3)_2$  with  $x = 0.10$ ,  
225 0.25 and 0.35.  $Cu^{2+}$ -doped hydrozincite exists as a natural aurichalcite  $(Zn_{1-x}Cu_x)_5(OH)_6(CO_3)_2$  ( $x = 0.24 - 0.40$ )  
226 mineral. Zheng et al. (Zheng et al. 2015) reported the structural analysis of synthetic  $Cu^{2+}$ -doped hydrozincite with  $x$   
227 = 0.1, 0.2, 0.3, 0.4 and 0.5. They demonstrated, using first-principal calculations, that  $Cu^{2+}$ -doped HZ materials  
228 maintain the original HZ structure with very low distortion and display a better thermodynamic stability than pure  
229 HZ.

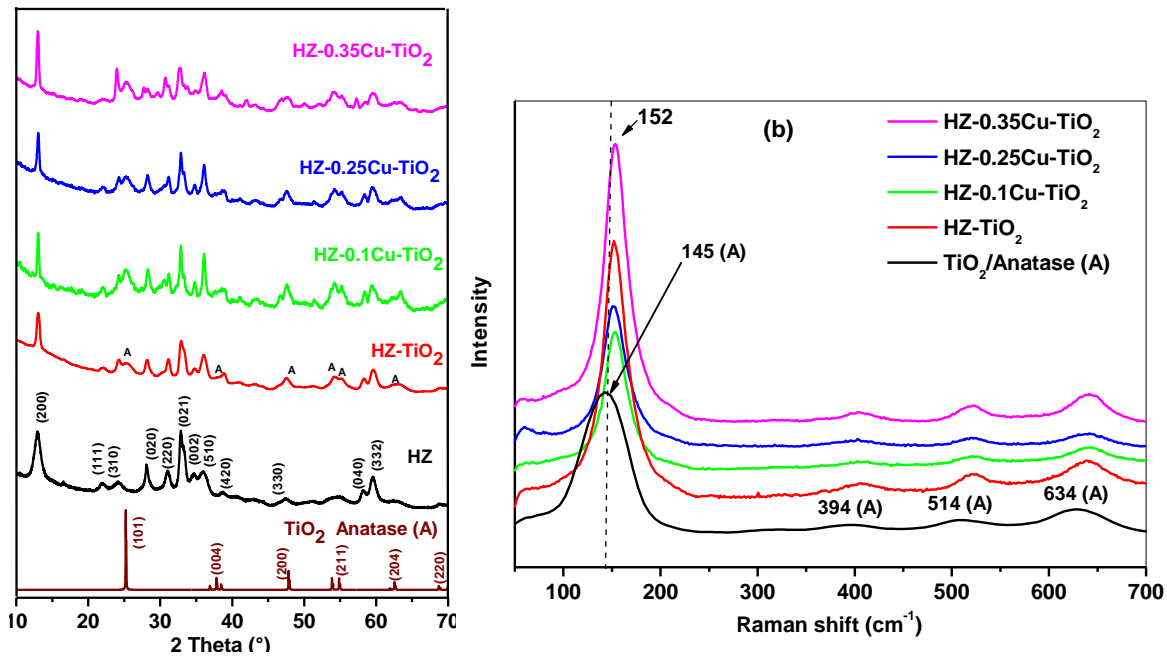
230 **Table 1.** Lattice parameters for the as-prepared materials.

Sample	a(Å)	b(Å)	c(Å)	Angle $\beta(^{\circ})$	Vcell(Å <sup>3</sup> )
x=0	13.62	6.35	5.41	96.24	465.4
x=0.1	13.62	6.34	5.40	96.42	463.1
x=0.25	13.63	6.33	5.40	96.21	463.6
x=0.35	13.61	6.32	5.40	96.20	461.9

231  
232 **Figure 1b** shows Raman spectra in the low-frequency region of the prepared compounds.

233 The formation of  $TiO_2$  during the coprecipitation/hydrothermal process is clearly evidenced by the presence of five  
234 vibrational modes typical of the anatase phase, at  $145\text{ cm}^{-1}$  ( $E_{g1}$ ) symmetric stretching vibration of O-Ti-O;

235  $394\text{ cm}^{-1}$  ( $E_{g2}$ );  $514\text{ cm}^{-1}$  ( $B_{g1}$ ) symmetrical flexion;  $634\text{ cm}^{-1}$  ( $A_{g1} + B_{g1}$ ) antisymmetric flexion (Pava-Gómez et al.  
 236 2021). However, for the HZ-TiO<sub>2</sub> and HZ-xCu-TiO<sub>2</sub> nanocomposites we note the presence of the same vibrational  
 237 modes as those for anatase, except for the fact that these were slightly shifted towards higher energy. This may  
 238 account for a doping effect of TiO<sub>2</sub> by Zn<sup>2+</sup>/Cu<sup>2+</sup> ions as reported by K. Assaker (Assaker et al. 2014). Moreover, the  
 239 displacement of the Eg(1) band is directly linked to the size of the TiO<sub>2</sub> crystallites (Kelly et al. 1997). Taking into  
 240 account the shift observed in our case ( $145\text{ cm}^{-1}$  for TiO<sub>2</sub> vs  $152\text{ cm}^{-1}$  for all TiO<sub>2</sub>/HZ nanocomposites), we can  
 241 deduce that the formed anatase is nanocrystalline with a particle size independent of the copper content (Jiang et al.  
 242 2021).



243 **Fig.1.** XRD patterns (a) and Raman spectra (b) of the synthesized composite materials and TiO<sub>2</sub> anatase.

### 244 3.1.2 UV-Vis diffuse reflection spectroscopy

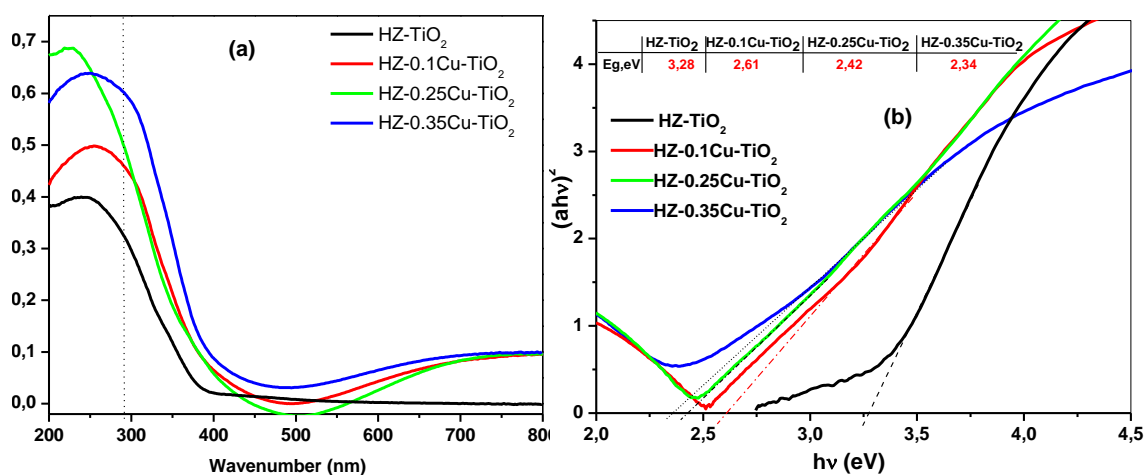
245  
 246 The UV-Vis diffuse absorption spectroscopy was used to study the influence of copper doping concentration and to  
 247 evaluate the band gap energies ( $E_g$ ) of the composite materials. The band gap energy has been calculated using the  
 248 Tauc equation (eq-6):  
 249

$$250 \quad (\alpha h\nu)^2 = K(h\nu - E_g) \quad (\text{Eq.6})$$

251 Where  $K$ ,  $h\nu$ ,  $\alpha$  and  $E_g$  represent the proportionally constant, the photon energy, the absorption coefficient, and the  
 252 band gap energy, respectively. The band gap energy can be estimated by extrapolating the linear area of the graph  
 253  $(\alpha h\nu)^2$  to  $h\nu$ , as shown in Figure 2 (b).

254 The electronic spectra of HZ-TiO<sub>2</sub> and HZ-xCu-TiO<sub>2</sub> are shown in Figure 2(a). The HZ-TiO<sub>2</sub> sample exhibits a  
 255 broad absorption band in the spectral range lower than 375 nm with a absorption maximum at 244 nm. This

256 spectrum can be attributed to the presence of TiO<sub>2</sub>, since several studies have shown that the absorbance of  
 257 hydrozincite does not exceed 250 nm (Turianicová et al. 2016; Cherepanova et al. 2017b; Liu and Teng 2018b;  
 258 Tzompantzi-Flores et al. 2020). This absorption band is due to the charge transfer between conduction band of the  
 259 Ti<sup>4+</sup> metal cation and the valence band of the O<sup>2-</sup> ligand. However, a noticeable red shift toward the visible range of  
 260 this band was observed when HZ-TiO<sub>2</sub> was doped by Cu<sup>2+</sup> ions, probably due to the formation of oxygen vacancies  
 261 (Olowoyo et al. 2018). The UV-VIS spectra of HZ-xCu-TiO<sub>2</sub> samples show another absorption band, less intense, in  
 262 the region of 660-800 nm which can be ascribed to the <sup>2</sup>E<sub>g</sub>→<sup>2</sup>T<sub>2g</sub> electronic transition of the Cu<sup>2+</sup> (d<sup>9</sup>) ion, then  
 263 inferring the presence of Cu<sup>2+</sup> in an octahedral environment-  
 264 The E<sub>g</sub> values of HZ-TiO<sub>2</sub>, HZ-0.1Cu-TiO<sub>2</sub>, HZ-0.25Cu-TiO<sub>2</sub>, and HZ-0.35Cu-TiO<sub>2</sub>, calculated from the Tauc  
 265 plots, are 3.28 eV, 2.61eV, 2.42 eV and 2.34 eV, respectively. Indeed, the absorption rate of visible light gradually  
 266 increases with the increase in Cu<sup>2+</sup> doping rate, This doping promotes the visible absorption of HZ-TiO<sub>2</sub>, as we can  
 267 see in the inset of Figure 2-a, which can improve its application under sunlight (Wang et al. 2020).



268  
 269 **Fig. 2. (a)** UV-vis diffuse absorbance spectra, **(b)** Band gap energy of HZ-xCu-TiO<sub>2</sub> (x= 0, 0.1,0.25 and 0.35).  
 270

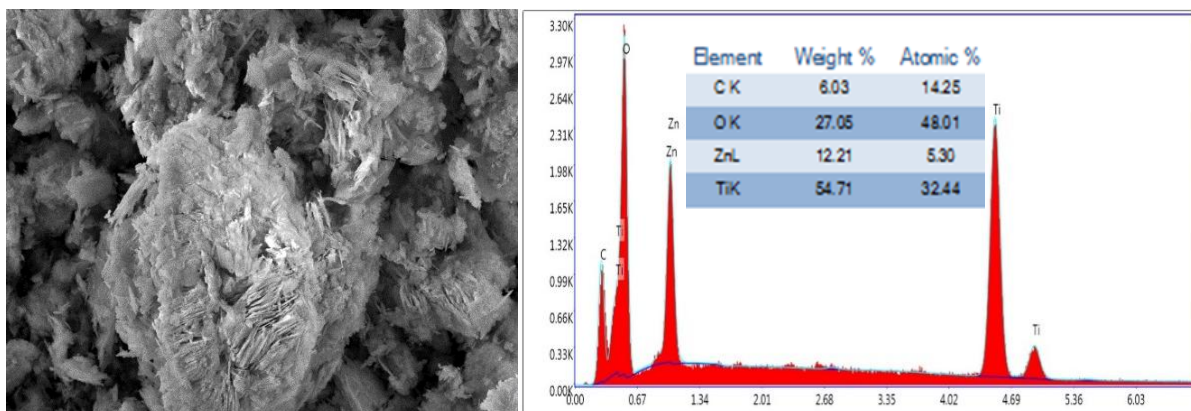
271 In the rest of this paper, we are going to focus the results of HZ-0.25Cu-TiO<sub>2</sub>: the most photoactive material  
 272 compared to other samples (vide infra).

### 273 3.1.3 SEM and EDX analysis

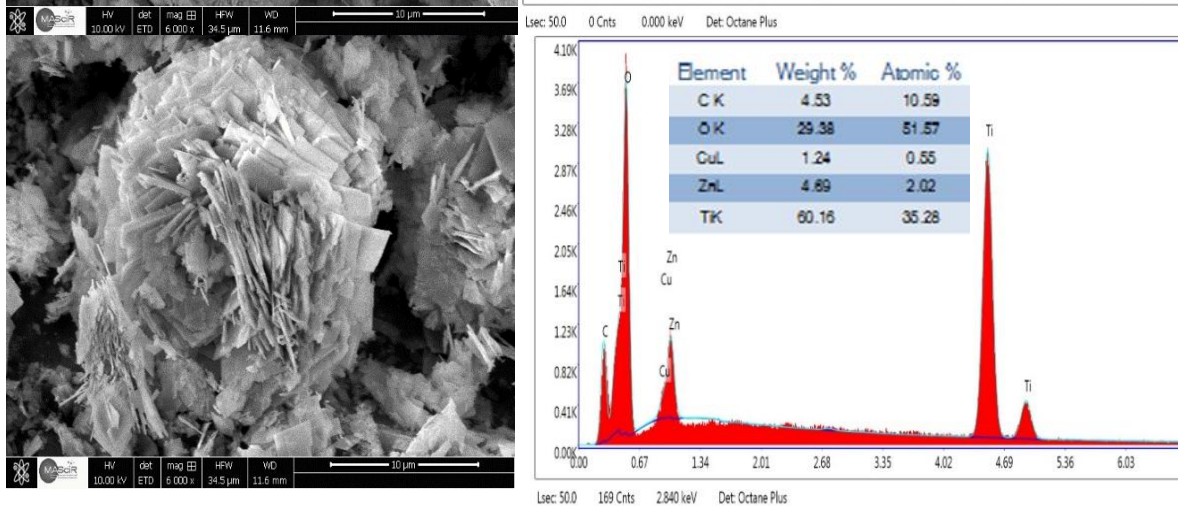
274 The morphology of HZ-TiO<sub>2</sub> and HZ-xCu-TiO<sub>2</sub> nanocomposites was characterized by SEM (Fig. 3a and b) and  
 275 TEM (Fig. 3c, de, e, f, and g). On the SEM images, both materials exhibit a hierarchical structure with many self-  
 276 assembled nanosheets in a flower-like morphology. This morphology is typical of hydrozincite compounds prepared  
 277 by urea-based precipitation method, as reported by Yan et al (Yan and Xue 2006b). Due to their small size, the  
 278 anatase nanoparticles are not distinguished on the SEM micrographs, while the existence of Ti in the sample is  
 279 clearly evidenced by EDX analysis. The TEM images of dispersed HZ-TiO<sub>2</sub> and HZ-xCu-TiO<sub>2</sub> samples clearly

280 evidence the presence of spherical nanoparticles of TiO<sub>2</sub> adsorbed at both the surface and the edge of the HZ-TiO<sub>2</sub>  
 281 layers (Fig. 3c, d, e and f). Elemental mapping (Fig. 3g) confirms the homogeneous distribution of Zn, Cu, O and C  
 282 over the HZ-xCu crystal while Ti is more scarcely distributed.

283



284

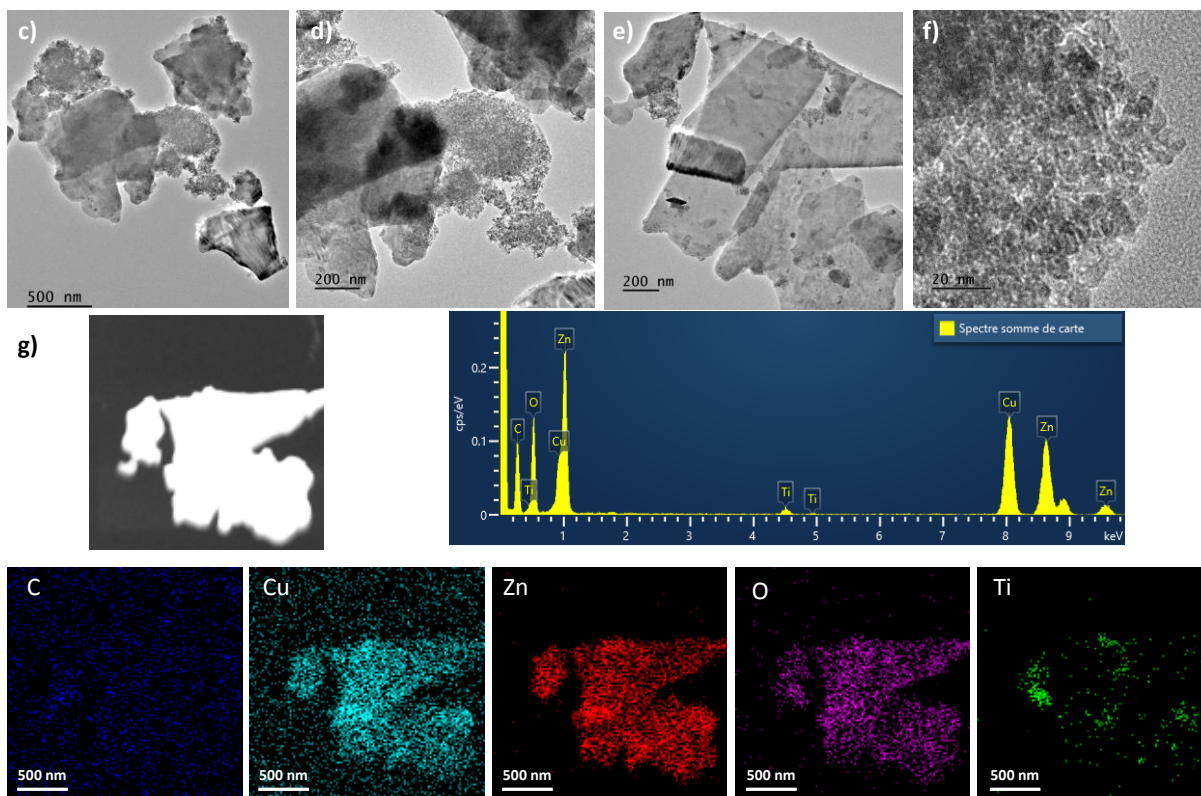


285

286

287

288



289

290

291 **Fig. 3.** SEM images (left), EDX spectrums (right) of HZ-TiO<sub>2</sub> (a) and HZ-0.25Cu-TiO<sub>2</sub> (b); TEM images of HZ-  
 292 TiO<sub>2</sub> (c & d) and HZ-0.25Cu-TiO<sub>2</sub> (e & f) and elemental mapping for HZ-0.25Cu-TiO<sub>2</sub>(g).

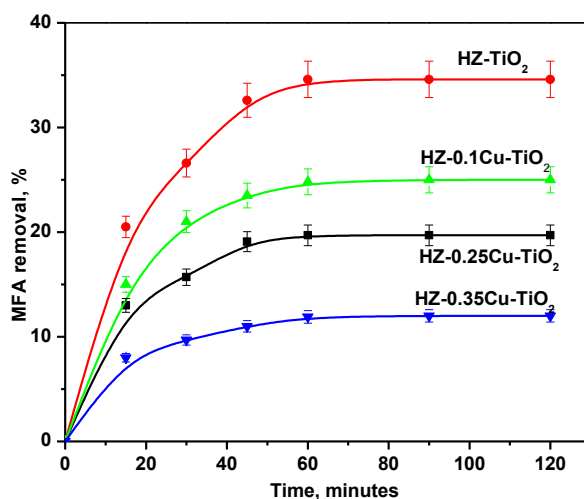
### 293 3.2 Adsorption study

#### 294 3.2.1 Contact time effect

295 The removal percentage (R %) of MFA ( $5.0 \times 10^{-5} \text{ mol.L}^{-1}$ ) by the sorbents ( $0.4 \text{ g.L}^{-1}$ ) at a contact time, t, was  
 296 estimated from the adsorption kinetic experiments, described in the experimental section, using the relationship :

$$297 R\% = \frac{C_i - C_t}{C_i} * 100 \quad (\text{eq.7})$$

298 Results are given in Fig. 4. For all sorbents, R% reaches a plateau corresponding at the equilibrium time of  
 299 adsorption,  $t_{\text{eq}}$ .  $t_{\text{eq}}$  was similar for all sorbents and equal to 70 min, time beyond which no more adsorption occurs.



300

301

**Fig. 4.** Adsorption kinetics of MFA by HZ-TiO<sub>2</sub> and HZ-xCu-TiO<sub>2</sub> LSHs adsorbents

302

(T 298 K; pH 7; C<sub>i</sub> = [MFA] = 5.0 × 10<sup>-5</sup> mol.L<sup>-1</sup>; [LSHs] = 0.4 g.L<sup>-1</sup>; and V = 50 mL).

303

The adsorption kinetics of mefenamic acid on the different LSHs was fitted using two models: pseudo-first-order model and pseudo-second-order model (Fig. SI.1). The pseudo-second-order model best describes (best R<sup>2</sup>) (Table 2) the kinetic behaviour of mefenamic acid adsorption by both LSHs, confirming that the mechanism controlling the adsorption rate is a chemical adsorption step.

307

**Table 2.** Kinetic parameters according to the pseudo second order and pseudo-first order models for the MFA adsorption.

308

	Pseudo-first-order			Pseudo-second-order		
	Q <sub>e</sub> (mg/g)	K <sub>1,ads</sub> (min <sup>-1</sup> )	R <sup>2</sup>	Q <sub>e</sub> (mg/g)	K <sub>2,ads</sub> (g.mg <sup>-1</sup> .mn <sup>-1</sup> )	R <sup>2</sup>
<b>HZ-0.25Cu-TiO<sub>2</sub></b>	8.13	0.092	0.917	6.85	0.02	0.987
<b>HZ-TiO<sub>2</sub></b>	9.33	0.052	0.891	13.89	0.004	0.990

309

### 3.2.2 Adsorption isotherms

311

The adsorption isotherms of MFA by HZ-TiO<sub>2</sub> and HZ-xCu-TiO<sub>2</sub> are plotted in Fig. SI.2 and the data processed from the Langmuir and Freundlich models are reported in table 3. Indeed, isotherm curves were analyzed using these two standard models in order to gain insight in the mechanism of MFA adsorption by the as-prepared sorbents. A comparison between the values of the regression coefficients of the Langmuir and Freundlich isotherms for MFA, shows that the Langmuir isotherm is the best model that describes well the equilibrium data and shows that the adsorbent material has a homogeneous surface. In addition, adsorption takes place by the creation of a monolayer of MFA covering the surface of the adsorbent with a correlation coefficient greater than 0,99.

316

317

318 With an octanol/water partition coefficient  $\log K_{ow} = 3.745$ , mefenamic acid has an intermediate  
 319 hydrophylic/lipophilic balance and a poor solubility ( $41 \text{ mg}\cdot\text{L}^{-1}$  at pH 7 and  $25^\circ\text{C}$ ). Consequently, most of the  
 320 published papers on the adsorption of MFA, reported the use of hydrophobic solids such as micelle-clay complexes  
 321 (Shen et al. 2022) MOFs (Wei et al. 2020) or activated carbon (Rueda-Márquez et al. 2021) for MFA adsorption.  
 322 Under our experimental conditions (pH = 6.8), MFA ( $pK_a = 4.2$ ) is in the anionic form  $\text{MFA}^-$  and adsorb at  
 323 hydroxylated surface or may complex surface cations. Adsorption experimental data (Fig. 4) show that the  
 324 MFA/LSH adsorption equilibrium were reached after 70 min. Maximum adsorption rates (%) calculated at 70 min  
 325 decrease in the series  $\text{HZ-TiO}_2(34.7\%) > \text{HZ-0.1Cu-TiO}_2(25.0\%) > \text{HZ-0.25Cu-TiO}_2(19.9\%) > \text{HZ-0.35Cu-TiO}_2$   
 326  $(12.2\%)$  (Fig. 4). Obviously, the decrease of MFA adsorption arises from the doping of  $\text{Cu}^{2+}$ . On the one hand,  
 327 because the quantity of  $\text{TiO}_2$  during synthesis is kept constant, and on the other hand, the adsorption of MFA by  
 328  $\text{TiO}_2$  does not exceed not 2.5% (Chen et al. 2016b). However, from adsorption isotherm data of MFA by  
 329 nanocellulose load with various amounts of  $\text{TiO}_2$  NP (Rathod et al. 2018), it was clear that the adsorption capacity  
 330 of nanocomposites decreases when increasing the rate of  $\text{TiO}_2$  loading, indicating that molecular interactions  
 331 between MFA and  $\text{TiO}_2$  surface are probably weak. We may conclude that adsorption properties of HZ toward MFA  
 332 are altered by the doping of  $\text{Cu}^{2+}$ .

333

334 **Table 3.** Parameters of Langmuir and Freundlich equations isotherms of  $[\text{MFA}] = 2$  to  $20 \text{ mg/L}$ ,  $[\text{LSHs}] = 0.4 \text{ g/L}$ ,  
 335  $T = 25^\circ\text{C}$ .

336

Langmuir model			Freundlich model			
	$Q_{\max}$ (mg/g)	$K_L$ (L/mg)	$R^2$	$K_f(\text{mg/g})$ (L/mg) <sup>1/n</sup>	1/n	$R^2$
<b>HZ-TiO<sub>2</sub></b>	28.5	0.23	0.99	2.58	1.36	0.96
<b>HZ-0.25Cu-TiO<sub>2</sub></b>	13.08	0.08	0.99	2.42	1.67	0.97

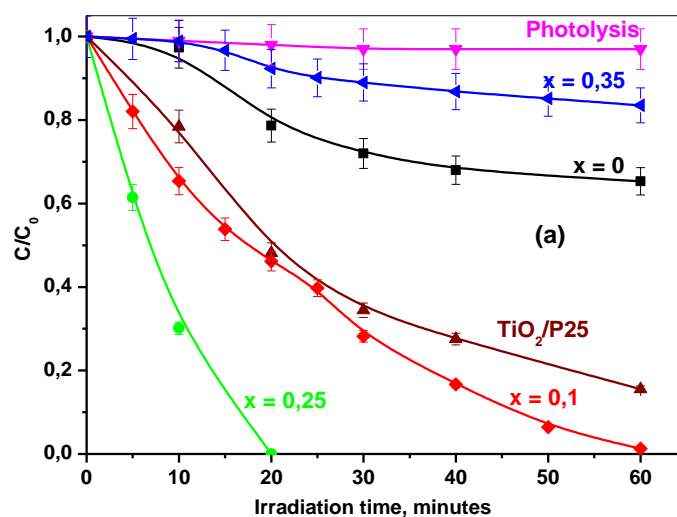
337

338 **3.3**

339 **Pho**

### 340 photocatalytic studies.

341 Direct photolysis processes can lead to a total or partial degradation of organic compounds in the medium by the  
 342 interaction between light and these pollutants (Rafqah and Sarakha 2016; EL Mersly et al. 2022). To answer this  
 343 hypothesis, we studied the effect of irradiation on the MFA solution without photocatalysts. According to the curve  
 344 shown in **Fig.5**, no loss of the pollutant is observed during 60 minutes of irradiation. This indicates that under our  
 345 experimental conditions, the pharmaceutical product MFA has a high photochemical stability.



347 **Fig.5.** Kinetics of MFA photocatalytic degradation (UV-Vis irradiation) (a)  
 348 ([MFA] =  $5.0 \times 10^{-5} \text{ mol.L}^{-1}$ , [photocatalyst] =  $0.40 \text{ g.L}^{-1}$ , pH=6.8).

346

347

348

349

350 Under the same conditions, the aqueous solution of MFA is magnet ically stirred for 60 minutes in dark conditions  
 351 to obtain the adsorption-desorption equilibrium. Afterwards, we proceeded to irradiate the pollutant in the presence  
 352 of HZ-xCu-TiO<sub>2</sub> composite (x=0; 0.1; 0.25 and 0.35) and in the presence of TiO<sub>2</sub>-P25 as reference photocatalyst.  
 353 According to the results obtained (**Fig.5**), HZ-0.25Cu-TiO<sub>2</sub> composite have a remarkable ability to induce  
 354 photochemical degradation of MFA in aqueous solution. It reaches an elimination rate equal to 100% during 20  
 355 minutes and this photoactivity is very superior compared to that of Degussa P25, compound well known for its wide  
 356 application in the field of photocatalysis.

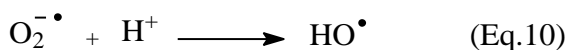
357 The interpretation of these results has been mentioned in several studies (Lin and Frei 2005a, b; Nakamura and Frei  
 358 2006; Lee et al. 2011), introducing the effect of the metal oxo-bridge structure M-O-M' into the mechanism of the  
 359 photocatalytic cycle. Indeed, the metal bridge incorporates the concept of metal-to-metal charge transfer (MMCT)  
 360 under light excitation. This new structure obtained by inserting copper into HZ-TiO<sub>2</sub>, implements new levels of  
 361 energy within the prohibited band, allowing for a allowing extension of the photoactive region especially in the  
 362 visible light range. This was confirmed by the photocatalytic efficiency of the HZ0.25Cu-TiO<sub>2</sub> composite in this  
 363 area (Fig SI-3).

364 It turned out, as shown in the literature for Cu<sup>2+</sup><sub>x</sub>-TiO<sub>2</sub> (), that the Cu<sup>2+</sup> doping in HZ-TiO<sub>2</sub> reduces the (e<sup>-</sup>/h<sup>+</sup>)  
 365 recombination rate and improve the charge carriers' availability of HZ-0.25Cu-TiO<sub>2</sub> nanoparticles (Eq.8).

366 Then, the Cu<sup>+</sup> react with adsorbed O<sub>2</sub> (Eq.9) by forming superoxide, which in turn can give rise to OH radicals  
 367 (Eq.10). With the decrease of electrons in the particles, the probability of charge recombination decreases and the



368 photocatalytic process becomes more efficient. This explanation is consistent with those mentioned by several  
 369 authors (Papp et al. 1993; Sreethawong and Yoshikawa 2005; Liu et al. 2017).



370

371 However, when the Cu concentration exceeds the value of  $x = 0.25$ , a significant decrease in photoactivity is  
 372 observed. The same results have been obtained in the literature (Di Paola et al. 2002, 2004). This inhibition of  
 373 photocatalytic activity can be attributed to an excessive absorption of light by copper with a high ratio, creating a  
 374 shielding effect. Moreover, a too high doping rate creates centers of recombination because of the decrease of the  
 375 average distance between the trapping sites (Liu et al. 2017).

376 From the graphical representation of the equation  $\ln(C/C_0)=f(t)$ , it is clear that the photocatalytic degradation of  
 377 MFA, during the first minutes of irradiation, follows a linear equation passing through the origin which effectively  
 378 corresponds to an apparent first order reaction rate constant (**Fig. SI.4**). The evolution of the concentration makes it  
 379 possible to determine the half-life time of the pollutant in each case. The values of the apparent rate constants and  
 380 half-life obtained are given in **Table 4**. Based on the above results, the apparent rate constant for the photocatalytic  
 381 degradation of the pharmaceutical product in the presence of composite material is the highest especially in the case  
 382  $x = 0.25$ , which presents exceptional values.

383

**Table 4.** Apparent rate Constants of and half-life times of MFA photocatalytic degradation.

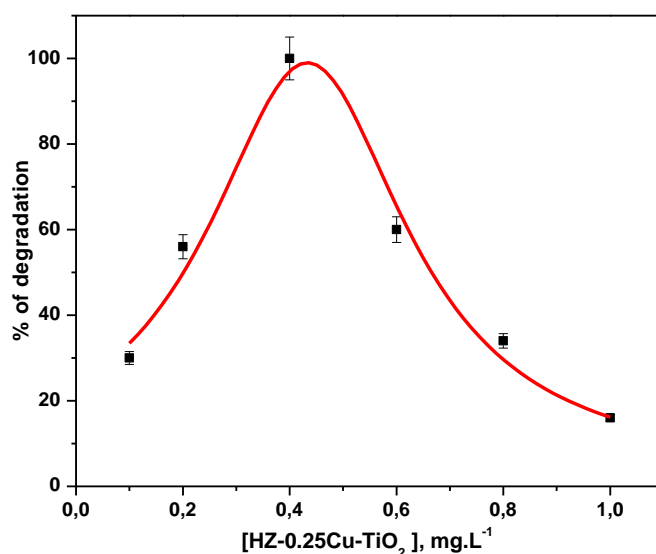
LDH	Degradation (%) at 20min	$k_{app} \times 10^2, \text{min}^{-1}$	$t_{1/2}, \text{min}$	$R^2$
HZ-TiO <sub>2</sub>	21.33	1.06	65.39	0.99
HZ-0.1Cu-TiO <sub>2</sub>	53.87	4.00	17.96	0.98
HZ-0.25Cu-TiO <sub>2</sub>	<b>100</b>	<b>11.55</b>	<b>6.00</b>	<b>0.99</b>
HZ-0.35Cu-TiO <sub>2</sub>	7.70	0.37	187.34	0.99
TiO <sub>2</sub> -P25	51.84	3.50	19.80	0.99

384

#### 385 3.4. Study of the photocatalytic performance by HZ-0.25Cu-TiO<sub>2</sub> different doses.

386 The influence of the amount of photocatalyst on the degradation of MFA was studied by varying the concentration  
 387 between 0.1 and 1.0 mg.L<sup>-1</sup>. Indeed, by increasing the concentration of the photocatalyst the efficiency of MFA  
 388 pharmaceutical pollutant removal is significantly improved. As shown in **Fig.6**, when the dose was increased from  
 389 0.1 to 0.4 mg.L<sup>-1</sup>, the removal efficiency increased from 32% to 100% in 20 minutes of irradiation. This can be  
 390 explained by the increase in the active sites of **HZ-0.25Cu-TiO<sub>2</sub>** composite.

391 On the other hand, a decrease in the percentage of degradation is observed for an amount of composite equal to 1  
392 mg.L<sup>-1</sup>. This phenomenon can also be observed due to an inner filter effect following the scattering of the incident  
393 light, when the concentration of composite was greater than 0.4 mg.L<sup>-1</sup> (EL Mersly et al. 2021).



394

395 **Fig.6.** Influence of HZ-0.25Cu-TiO<sub>2</sub> concentration on the percentage of MFA photocatalytic degradation, pH=6.8.

### 396 3.6. Effect of pH

397 pH of the solution represents an important factor in the photocatalytic process by modifying the surface charge of  
398 photocatalyst and ionic forms of pollutants. The photocatalytic degradation of MFA was studied in acidic, neutral  
399 and alkaline environments by adding NaOH (basic pH) or HClO<sub>4</sub> (acidic pH).

400 The kinetic curves (**Fig. SI.5**) show the degradation under different pH values. It is noted that the rate of degradation  
401 increases slightly with increasing pH, this can be explained by the increase in the number of hydroxyl radicals (OH<sup>•</sup>)  
402 generated and favored at alkaline pH. However, this degradation of MFA in a basic medium is not very significant;  
403 it remains low compared to that reported in several studies. Therefore, we assume that increasing the pH can  
404 promote the formation of aggregates that are less sensitive to light (EL Mersly et al. 2021). Subsequently, the effect  
405 of the light excitation can form only very few hydroxyl radicals, photogenerated from the OH<sup>-</sup> ions. As a result, the  
406 photocatalytic efficiency is not very important in this medium. The table 5 shows the rate constants of degradation  
407 of MFA catalyzed by HZ-0.25Cu-TiO<sub>2</sub> under different pH conditions. According to these results, it can be seen that  
408 the rate constant of degradation changes from 0.1013 to 0.1598 when the pH value changes from 4 to 9. As the pH  
409 increases, the MFA appears more in anionic form in the system. This ionic form of MFA increases the density of the  
410 electron clouds of the benzenic cycle. As a result, MFA would become more susceptible to attack by hydroxyl  
411 radicals (Chen et al. 2015)

412

413 **Table 5.** Degradation kinetics and correlation constants for photocatalytic degradation of MFA under different pH  
 414 conditions.

	Constants $k_{app} \cdot 10^2$ ( $\text{min}^{-1}$ )	Half-time $t_{1/2}$ (min)	Correlation ( $R^2$ )
<b>pH 4.0</b>	10.13	6.84	0.98
<b>pH 6.8</b>	13.22	5.24	0.98
<b>pH 9.0</b>	15.98	4.34	0.97

415

### 416 3.7. Effect of positive hole and radical hydroxide

417 Several studies have demonstrated that  $\text{HO}^\bullet$  hydroxyl radicals are the main species responsible for the degradation  
 418 of organic pollutants in aqueous solution via oxidation reactions (Meribout et al. 2016; El Mouchtari et al. 2020).

419 However, some works have also shown the key role of holes ( $\text{h}^+$ ) in the photocatalytic process (Meribout et al. 2016;

420 EL Mersly et al. 2021). To elucidate the nature of the reactive species and their impact in the photodegradation of

421 MFA, we proceeded first to the irradiation of the solutions in the presence of isopropanol which is described as the

422 best inhibitor for  $\text{HO}^\bullet$  (Meribout et al. 2016; El Mouchtari et al. 2021). As can be seen in **fig.7 (a)**, the degradation of

423 MFA decreases in the presence of isopropanol in the medium. The degradation percentage is of the order of 48.28%

424 ( $k=2.94 \times 10^{-2} \text{ mn}^{-1}$ ) in the presence of 2% of isopropanol. This amount is sufficient to inhibit almost all the generated

425 hydroxyl radicals. Excitation in the presence of isopropanol confirms that hydroxyl radicals are not the only species

426 responsible for the degradation of MFA. For this, we studied the effect of triethanolamine ( $[\text{TEOA}]=1.0 \text{ mmol.L}^{-1}$ )

427 on the photocatalytic degradation of MFA in the presence of HZ-0.25Cu-TiO<sub>2</sub>. This product is well known for its

428 ability to inhibit holes ( $\text{h}^+$ ), which leads, by electron transfer to the formation of the TEOA<sup>+</sup> cation radical.

429 To confirm the holes involvement in the photodegradation reaction, a mixture (MFA/HZ-0.25Cu-TiO<sub>2</sub>) containing

430  $1.0 \text{ mmol.L}^{-1}$  of triethanolamine was irradiated under the same conditions. The results of **Fig.7(b)** show that the

431 percentage of photocatalytic degradation of MFA decreases from 100 to 85% ( $k=4.11 \times 10^{-2} \text{ mn}^{-1}$ ) in the presence of

432 triethanolamine. All these results imply that the hydroxyl radicals and holes  $\text{h}^+$  are the principal species involved in

433 the degradation of the MFA.

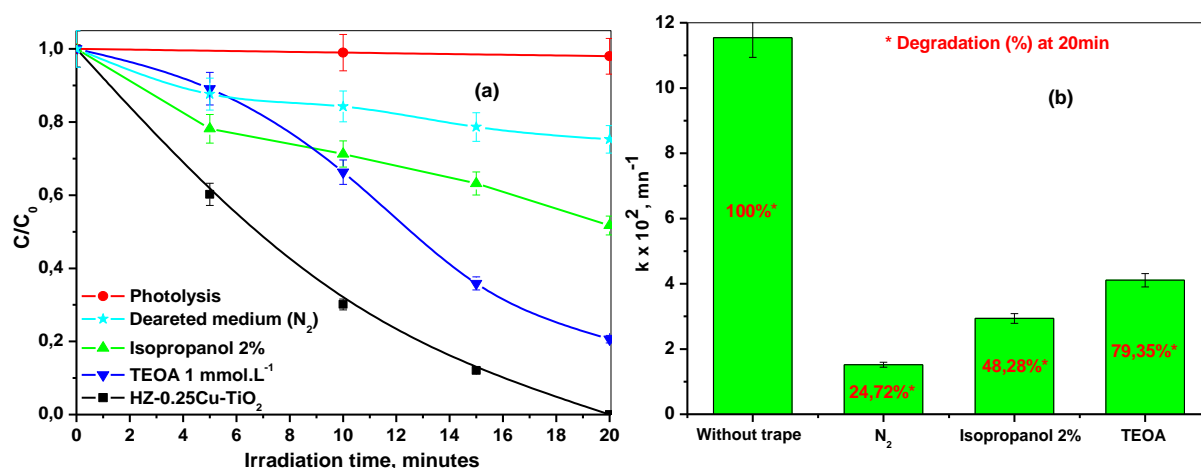
434 In order to study the involvement of oxygen in the photocatalytic process, the MFA solution was bubbled with

435 nitrogen, in the presence of HZ-0.25CuTiO<sub>2</sub>, throughout the duration of the irradiation under the same experimental

436 conditions. It was found that the photocatalytic degradation of MFA was significantly affected by absence of O<sub>2</sub>

437 since the percentage of degradation did not exceed 24.72% ( $k 1.52 \times 10^{-2} \text{ mn}^{-1}$ ). This suggests that oxygen plays a

438 major role in the MFA degradation.



439

440 **Fig.7.** MFA degradation kinetic (a) and rate constants of degradation of MFA in the presence of some  
 441 photocatalytic activity inhibitors ( $[MFA]= 5.0 \times 10^{-5} \text{mol.L}^{-1}$ ,  $[HZ-0.25\text{Cu-TiO}_2] = 0.4 \text{mg.L}^{-1}$ ).  
 442

### 443 3.8. Analytical study

444 MFA solution were irradiated in the presence of HZ-0.25Cu-TiO<sub>2</sub> during 5min (**Fig. SI.6**). We limited the  
 445 photodegradation process to relatively short times in order to be able to analyze primary intermediate products. The  
 446 formed photoproducts were detected using high-resolution mass spectrometry coupled with liquid chromatography  
 447 (LC-MS) in positive mode. First, we were interested in identifying the exact mass of each photoproduct; this step  
 448 allows us to propose a raw formula presented below.

449

#### 450 3.8.1. Identification of photoproducts resulting

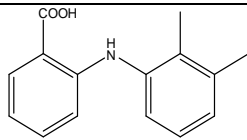
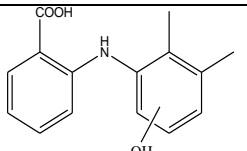
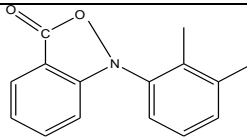
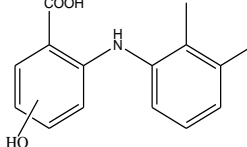
451 The characterization of the MFA and their photoproducts was carried out by the HPLC-MS<sup>2</sup> technique.  
 452 Identification of photoproducts, as well as their structures, were based on the mass spectrometry experiments carried  
 453 out in positive ion mode (ESI+) and on comparison with literature data, including studies on photoproducts obtained  
 454 from mefenamic acid and others of the same family, subjected to the photolysis and/or the photodegradation-  
 455 induced in aqueous solution (Pérez-Estrada et al. 2005; Chen et al. 2015, 2016a; de Melo da Silva et al. 2016). The  
 456 MFA drug ( $t_r = 7.62$  minutes) gives a mass value at  $m/z = 242$  ( $C_{15}H_{16}NO_2^+$ ) as well as a daughter fragment ion at  
 457  $m/z = 224$  and 181. The latter corresponds to the loss of a water molecule and (-CO-CH<sub>3</sub>) group, respectively.

458 The photoproduct P1 which appeared at 6.22 min was identified with a mass  $m/z$  258, corresponding to the addition  
 459 of a mass of 16 units to the MFA product with an elementary composition  $C_{15}H_{16}NO_3$ . It is a hydroxylation of the  
 460 aromatic ring containing the bi-methyl groups having an electron donating effect. On the other hand, the presence of  
 461 three free positions probably leads to the formation of three isomers, with very close retention times, one of which is  
 462 predominant, in particular at the Para position of the nitrogen. MSMS analysis of this photoproduct leads to the

463 formation of two fragments  $m/z$  equal to 240 and 160. They correspond respectively to the loss of a group of an  $H_2O$   
 464 molecule and of the  $-C_5H_4O$  group obtained after opening of the aromatic ring.  
 465 Two other hydroxylated products, of  $m/z = 258$  appeared at 4.00 and 3.08 minutes. This hydroxylation can only take  
 466 place on the other aromatic ring, already approved by several authors (Vogna et al. 2004; Rafqah et al. 2006,  
 467 2015) Under the electron-withdrawing effect of the carboxylic function, this substitution is favored in the meta  
 468 position of this group.  
 469 The photoproduct (P4) detected at a retention time of 4.01 min, with a base peak of  $m/z$  240 in the corresponding  
 470 mass spectrum is due the loss of a unit to MFA. It turned out that it had a loss of a hydrogen following a cyclization;  
 471 the best fit for the elemental composition was chosen to be  $C_{15}H_{13}NO_2$ . The fragments generated by MSMS (225  
 472 and 210) are attributed to a loss of the two methyl groups.  
 473 The photoproduct (P5) detected at the highest intensity appeared at a retention time of 2.56 min. following its mass  
 474 of  $m/z$  180 an opening of the aromatic nucleus is possible. This was also confirmed by the fragments observed at  
 475 137 and 109 and which correspond to a loss of two groups  $-CH_2COH$  and  $-CH_2COH-CO$ , respectively.

476  
477

**Table 6.** MFA photocatalytic products in aqueous solution.

Compound ( $t_r$ , mn)	$[M+H]^+$ $m/z$	Masse difference	Molecular Formula	$[M+H]^+$ $MS^2$	Fragments of $MS^2$	Structure proposal
MFA (7.62)	242.1176	-	$[C_{15}H_{16}NO_2]^+$	224 181	$[C_{15}H_{14}NO_2]^+$ $[C_{13}H_{11}N]^+$	
P1 (6.22)	258.0295	+16	$[C_{15}H_{16}NO_3]^+$	240 160	$[C_{15}H_{16}NO_3]^+$ $[C_{10}H_{10}NO]^+$	
P2 (4.01)	240.0687	-2	$[C_{15}H_{14}NO_2]^+$	225 210	$[C_{14}H_{11}NO_2]^+$ $[C_{13}H_8NO_2]^+$	
P3 (3.08) P4 (2.56)	258.2277 258.1172	+16	$[C_{15}H_{16}NO_3]^+$	160 142	$[C_{10}H_{10}NO]^+$ $[C_{10}H_{12}N]^+$	

P5 (2.31)	180.0031	-62	$[\text{C}_9\text{H}_9\text{NO}_3+\text{H}]^+$	137 109	$[\text{C}_7\text{H}_7\text{NO}_2]^+$ $[\text{C}_6\text{H}_7\text{NO}]^+$	
-----------	----------	-----	--	------------	--	--

478

### 479 3.8.2. Degradation pathways and Mineralization of MFA.

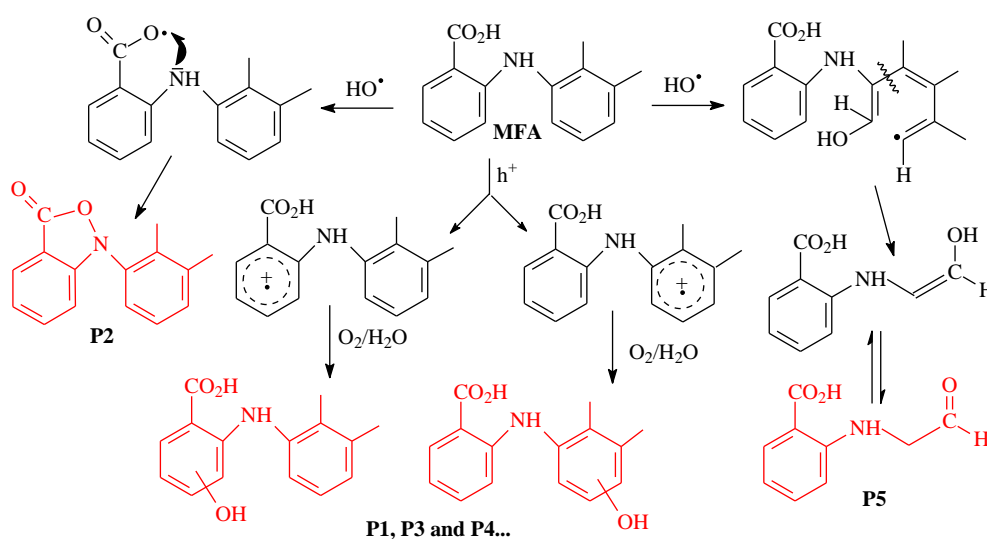
480 As shown in Scheme 1, the degradation products of MFA by HZ-0.25Cu-TiO<sub>2</sub> were produced by three types of  
481 reactions of hydroxylation, cyclization and cleavage of the aromatic ring.

482 In our case, an electron transfer process involving the aromatic ring I and h<sup>+</sup> results in the formation radical cation,  
483 consequently, a preferential attack of oxygen at this group forming subsequently the hydroxylated product P1.  
484 Similarly, on the aromatic ring II promotes reactivity with the oxygen, subsequently leading to the products P3 and  
485 P4. These results are in perfect agreement with the work carried out by De Melo da Silva *et al* (de Melo da Silva et  
486 al. 2016).

487 During the dehydrogenation (hydrogen-abstraction) of the carboxylic function by hydroxyl radicals, the O–H bond  
488 was broken and hydrogen was extracted to form a new O–H bond, leading to the formation of a molecule of water  
489 (Wu et al. 2017). It leads also to the formation of a radical that can easily react with the non-binding doublet of  
490 nitrogen, subsequently generating the cyclized product P2.

491 Following a radical addition of the ·OH group on the carbon in the Meta nitrogen position, which seems to be a  
492 primary step in the reactivity, it initially allows to initiate its opening. The presence of the superoxide anion O<sub>2</sub><sup>·-</sup>,  
493 formed during the photocatalytic cycle, and of the H<sup>+</sup> ions from the medium, makes it possible to obtain the final  
494 product (P5).

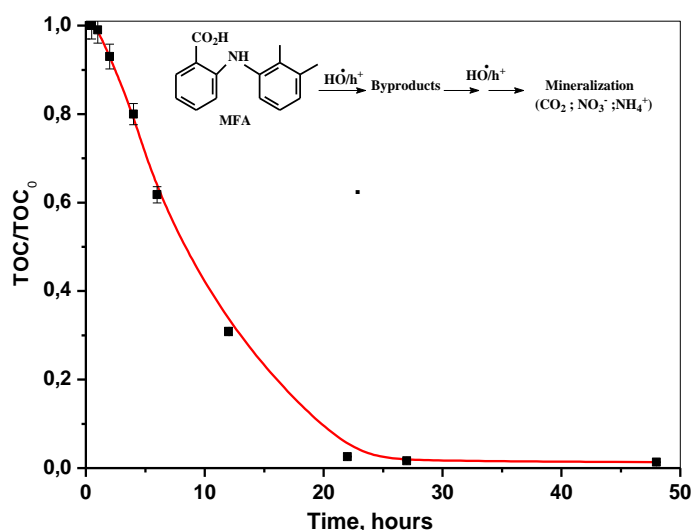
495



496

497 **Scheme 1.** Photocatalytic degradation pathways of MFA in the presence of HZ-0.25Cu-TiO<sub>2</sub>.

498 The kinetics of the total MFA mineralization was monitored in the aqueous phase using total organic carbon (TOC)  
499 analysis. As depicted in **Fig.8**, a decrease in TOC was effective from the early stages of irradiation to total  
500 mineralization at 24 hours. Total MFA mineralization (100% rate) is reached after 22 hours, with the disappearance  
501 of MFA and all the photoproducts obtained at the beginning of the photocatalytic process (20 min). The above  
502 results enable us to confirm that the HZ-0.25Cu-TiO<sub>2</sub> nanocomposite is very effective in completely mineralizing  
503 such organic pollutants.



504

505 **Fig.8.** The evolution of TOC as a function of irradiation time: [MFA] =  $5.0 \times 10^{-5} \text{ mol.L}^{-1}$ .

506

[HZ-0.25Cu-TiO<sub>2</sub>] = 0.4 mg.L<sup>-1</sup>.

507

### 3.10. Recycling and reuse

508 During the stability study and the reuse of the photocatalyst, the degree of MFA degradation for the first cycle was  
509 100% (**Fig.9**). Although the catalyst's degradation capacity decreased after several cycles, the degradation rate was  
510 still 90% after the sixth cycle. It can be seen that our sample shows only a 10% change in activity after 6 repeated  
511 uses, which may be due to the loss of mass after each cycle. During a study conducted on recycling Hydroxide-TiO<sub>2</sub>  
512 nanocomposites, the authors reported that the degradation rates do not exceed 56% and after six recycling tests that  
513 the reduced photocatalytic efficiency to 41.9% (Contreras-Ruiz et al. 2017). However, this study discovered that our  
514 material maintained its photocatalytic properties and showed ease of regeneration. The nanocomposite used in this  
515 work can serve as an example for further developing more stable and efficient photocatalysts that can recycled by  
516 simple filtration. It could be admitted as an encouraging photocatalyst with high activity, long-term durability, and  
517 excellent recyclability.

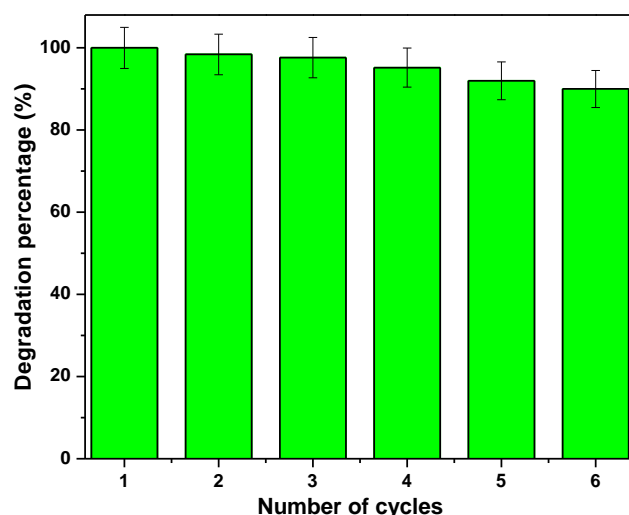


**Fig.9.** Reuse of HZ-0.25Cu-TiO<sub>2</sub> material for MFA removal ([MFA] = 5.0 x 10<sup>-5</sup> mol.L<sup>-1</sup>, [photocatalyst] = 0.4g.L<sup>-1</sup>)

518

519

520

### 521 **Conclusion**

522 In summary, HZ-xCu-TiO<sub>2</sub> (x= 0; 0.1; 0.25; 0.35) have been successfully prepared by the urea method. The  
 523 prepared composite materials have shown good adsorption capacity for mefenamic acid. The adsorption process  
 524 follows a Langmuir-type isotherm, which explains why the adsorption of our pollutant was carried out in a  
 525 monolayer.

526 The study of photocatalytic efficiency tested on mefenamic acid showed that HZ-0.25Cu-TiO<sub>2</sub> is the most  
 527 photoactive. The elimination rate is obtained for 20 minutes. This photocatalytic activity of HZ-0.25Cu-TiO<sub>2</sub> is  
 528 correlated to its lower bandgap (~2.42 eV), its structural properties, and also the copper doping which allowed the  
 529 extension of the photoactive region especially in the visible light range.

530 The stability and reusability of the catalyst was also investigated. The results showed the regeneration of HZ-  
 531 0.25Cu-TiO<sub>2</sub> and its activity has been preserved during six consecutive cycles. This allows us to consider this new  
 532 composite material as a promising photocatalyst, with high activity, long-term durability, and excellent applicability  
 533 for wastewater treatment.

534

### 535 **Declaration of Competing Interest**

536 The authors declare no competing financial interest.

### 537 **Availability of data and materials**

538 In this current research, the datasets obtained and analyzed are available with the corresponding author, “Ms Lekbira  
 539 El Mersly.”

540

### 541 **Authors Contributions**

542 Lekbira EL Mersly: Investigation, Resources, Writing - original draft

543 El Mountassir El Mouchtari: Data curation, Methodology

544 El Mostafa Moujahid: Supervision,

545 Claude Forano: Validation, Writing-review and editing

546 Samir Briche: Resources

547 Abdelaaziz Alaoui Tahiri: Validation.



548 Salah Rafqah: Supervision, Writing - review and editing.  
549

550 **Ethical Approval and Consent to Participate**

551 The paper does not involve relevant ethical research.  
552

553 **Consent to Publish**

554 No conflict interest exists in the submission of this manuscript, and manuscript is approved by all authors for  
555 publication. The work described was original research that has not been published previously, and not under  
556 consideration for publication elsewhere, in whole or in part. All the authors listed have approved the manuscript that  
557 is enclosed.

558 **Acknowledgements**

559 The authors gratefully acknowledge “Centre d'Analyse et de Caractérisation (CAC), université Cadi Ayyad » and  
560 Centre National pour la Recherche Scientifique et Technique » (CNRST-Morocco) for his financial support (Merit  
561 scholarship. Code: 8UCA2019).  
562

563

564

565

566

567

568

569

570

571

572

573

574

575

576

577

578

579

580

581

582

583 **References**

- 584 Abdolmohammad-Zadeh H, Morshedzadeh F, Rahimpour E (2014) Trace analysis of mefenamic acid in human  
585 serum and pharmaceutical wastewater samples after pre-concentration with Ni–Al layered double  
586 hydroxide nano-particles. *Journal of Pharmaceutical Analysis* 4:331–338.  
587 <https://doi.org/10.1016/j.jpha.2014.04.003>
- 588 Ansari R, Mosayebzadeh Z (2010) Removal of Eosin Y, an Anionic Dye, from Aqueous Solutions using Conducting  
589 Electroactive Polymers. *Polymer Journal* 541–551
- 590 Araujo L, Villa N, Camargo N, et al (2011) Persistence of gemfibrozil, naproxen and mefenamic acid in natural  
591 waters. *Environ Chem Lett* 9:13–18. <https://doi.org/10.1007/s10311-009-0239-5>
- 592 Assaker K, Carteret C, Roques-Carmes T, et al (2014) Influence of Zn ion addition on the properties of ordered  
593 mesoporous TiO<sub>2</sub>. *New J Chem* 38:2081. <https://doi.org/10.1039/c4nj00051j>
- 594 Chen P, Lv W, Chen Z, et al (2015) Phototransformation of mefenamic acid induced by nitrite ions in water:  
595 mechanism, toxicity, and degradation pathways. *Environ Sci Pollut Res* 22:12585–12596.  
596 <https://doi.org/10.1007/s11356-015-4537-0>
- 597 Chen P, Wang FL, Yao K, et al (2016a) Photodegradation of Mefenamic Acid in Aqueous Media: Kinetics, Toxicity  
598 and Photolysis Products. *Bull Environ Contam Toxicol* 96:203–209. <https://doi.org/10.1007/s00128-015-1680-8>
- 599
- 600 Chen P, Wang FL, Yao K, et al (2016b) Photodegradation of Mefenamic Acid in Aqueous Media: Kinetics, Toxicity  
601 and Photolysis Products. *Bull Environ Contam Toxicol* 96:203–209. <https://doi.org/10.1007/s00128-015-1680-8>
- 602
- 603 Cherepanova S, Markovskaya D, Kozlova E (2017a) Identification of a deleterious phase in photocatalyst based on  
604 Cd<sub>1-x</sub>Zn<sub>x</sub>S/Zn(OH)<sub>2</sub> by simulated XRD patterns. *Acta Crystallogr B Struct Sci Cryst Eng Mater* 73:360–  
605 368. <https://doi.org/10.1107/S2052520617001664>
- 606 Cherepanova S, Markovskaya D, Kozlova E (2017b) Identification of a deleterious phase in photocatalyst based on  
607 Cd<sub>1-x</sub>Zn<sub>x</sub>S/Zn(OH)<sub>2</sub> by simulated XRD patterns. *Acta Crystallogr B Struct Sci Cryst Eng Mater* 73:360–  
608 368. <https://doi.org/10.1107/S2052520617001664>
- 609 Colombo R, Ferreira TCR, Ferreira RA, Lanza MRV (2016) Removal of Mefenamic acid from aqueous solutions by  
610 oxidative process: Optimization through experimental design and HPLC/UV analysis. *Journal of*  
611 *Environmental Management* 167:206–213. <https://doi.org/10.1016/j.jenvman.2015.11.029>
- 612 Contreras-Ruiz JC, Martínez-Gallegos S, Ordoñez E, et al (2017) Synthesis of Hydroxide–TiO<sub>2</sub> Compounds with  
613 Photocatalytic Activity for Degradation of Phenol. *Journal of Elec Materi* 46:1658–1668.  
614 <https://doi.org/10.1007/s11664-016-5209-7>
- 615 de Melo da Silva L, Pereira Cavalcante R, Fabbro Cunha R, et al (2016) Tolfenamic acid degradation by direct  
616 photolysis and the UV-ABC/H<sub>2</sub>O<sub>2</sub> process: factorial design, kinetics, identification of intermediates, and  
617 toxicity evaluation. *Science of The Total Environment* 573:518–531.  
618 <https://doi.org/10.1016/j.scitotenv.2016.08.139>
- 619 Di Paola A, García-López E, Ikeda S, et al (2002) Photocatalytic degradation of organic compounds in aqueous  
620 systems by transition metal doped polycrystalline TiO<sub>2</sub>. *Catalysis Today* 75:87–93.  
621 [https://doi.org/10.1016/S0920-5861\(02\)00048-2](https://doi.org/10.1016/S0920-5861(02)00048-2)
- 622 Di Paola A, García-López E, Marci G, et al (2004) Surface characterisation of metal ions loaded TiO<sub>2</sub> photocatalysts:  
623 structure–activity relationship. *Applied Catalysis B: Environmental* 48:223–233.  
624 <https://doi.org/10.1016/j.apcatb.2003.10.015>

- 625 EL Mersly L, El Mouchtari EM, Moujahid EM, et al (2021) ZnCr-LDHs with dual adsorption and photocatalysis  
626 capability for the removal of acid orange 7 dye in aqueous solution. *Journal of Science: Advanced*  
627 *Materials and Devices* 6:118–126. <https://doi.org/10.1016/j.jsamd.2020.08.002>
- 628 EL Mersly L, EL Mouchtari EM, Zefzoufi M, et al (2022) Kinetics, mechanism studies and antibacterial activity of  
629 pharmaceutical Sulfaguanidine under light irradiation in aqueous solution. *Journal of Photochemistry and*  
630 *Photobiology A: Chemistry* 430:113985. <https://doi.org/10.1016/j.jphotochem.2022.113985>
- 631 El Mouchtari EM, Bahsis L, El Mersly L, et al (2021) Insights in the Aqueous and Adsorbed Photocatalytic  
632 Degradation of Carbamazepine by a Biosourced Composite: Kinetics, Mechanisms and DFT Calculations.  
633 *Int J Environ Res* 15:135–147. <https://doi.org/10.1007/s41742-020-00300-2>
- 634 El Mouchtari EM, Daou C, Rafqah S, et al (2020) TiO<sub>2</sub> and activated carbon of *Argania Spinosa* tree nutshells  
635 composites for the adsorption photocatalysis removal of pharmaceuticals from aqueous solution. *Journal*  
636 *of Photochemistry and Photobiology A: Chemistry* 388:112183.  
637 <https://doi.org/10.1016/j.jphotochem.2019.112183>
- 638 Fent K, Weston A, Caminada D (2006) Ecotoxicology of human pharmaceuticals. *Aquatic Toxicology* 76:122–159.  
639 <https://doi.org/10.1016/j.aquatox.2005.09.009>
- 640 Freundlich HMF (1906) über die adsorption in losungen (Adsorption in Solution). *Zeitschrift für Physikalische*  
641 *Chemie* 385–490
- 642 Ghose S (1964) The crystal structure of hydrozincite, Zn<sub>5</sub>(OH)<sub>6</sub>(CO<sub>3</sub>)<sub>2</sub>. *Acta Cryst* 17:1051–1057.  
643 <https://doi.org/10.1107/S0365110X64002651>
- 644 Gimeno O, Rivas J, Encinas A, Beltran F (2010) Application of Advanced Oxidation Processes to Mefenamic Acid  
645 Elimination. *Engineering and Technology International Journal of Nuclear and Quantum Engineering* 399–  
646 401
- 647 Gros M, Petrović M, Barceló D (2007) WASTEWATER TREATMENT PLANTS AS A PATHWAY FOR AQUATIC  
648 CONTAMINATION BY PHARMACEUTICALS IN THE EBRO RIVER BASIN (NORTHEAST SPAIN). *Environ Toxicol*  
649 *Chem* 26:1553. <https://doi.org/10.1897/06-495R.1>
- 650 Intissar M, Holler S, Malherbe F, et al (2004) Incorporation of Ti<sup>4+</sup> into layered double hydroxide sheets? The  
651 response by X-ray diffraction and absorption study. *Journal of Physics and Chemistry of Solids* 65:453–  
652 457. <https://doi.org/10.1016/j.jpics.2003.08.030>
- 653 Jaramillo-Páez C, Navío JA, Hidalgo MC, Macías M (2017) High UV-photocatalytic activity of ZnO and Ag/ZnO  
654 synthesized by a facile method. *Catalysis Today* 284:121–128.  
655 <https://doi.org/10.1016/j.cattod.2016.11.021>
- 656 Jiang K, Zhang J, Luo R, et al (2021) A facile synthesis of Zn-doped TiO<sub>2</sub> nanoparticles with highly exposed (001)  
657 facets for enhanced photocatalytic performance. *RSC Adv* 11:7627–7632.  
658 <https://doi.org/10.1039/D0RA09318A>
- 659 Jones OAH, Voulvoulis N, Lester JN (2006) Partitioning Behavior of Five Pharmaceutical Compounds to Activated  
660 Sludge and River Sediment. *Arch Environ Contam Toxicol* 50:297–305. <https://doi.org/10.1007/s00244-005-1095-3>
- 662 Kelly S, Pollak FH, Tomkiewicz M (1997) Raman Spectroscopy as a Morphological Probe for TiO<sub>2</sub> Aerogels. *J Phys*  
663 *Chem B* 101:2730–2734. <https://doi.org/10.1021/jp962747a>
- 664 Lee Y, Choi JH, Jeon HJ, et al (2011) Titanium-embedded layered double hydroxides as highly efficient water  
665 oxidation photocatalysts under visible light. *Energy Environ Sci* 4:914.  
666 <https://doi.org/10.1039/c0ee00285b>

- 667 Li J, Jin Z (2009) Effect of hypersaline aniline-containing pharmaceutical wastewater on the structure of activated  
668 sludge-derived bacterial community. *Journal of Hazardous Materials* 172:432–438.  
669 <https://doi.org/10.1016/j.jhazmat.2009.07.031>
- 670 Lin W, Frei H (2005a) Photochemical CO<sub>2</sub> Splitting by Metal-to-Metal Charge-Transfer Excitation in Mesoporous  
671 ZrCu(I)-MCM-41 Silicate Sieve. *J Am Chem Soc* 127:1610–1611. <https://doi.org/10.1021/ja040162l>
- 672 Lin W, Frei H (2005b) Anchored Metal-to-Metal Charge-Transfer Chromophores in a Mesoporous Silicate Sieve for  
673 Visible-Light Activation of Titanium Centers. *J Phys Chem B* 109:4929–4935.  
674 <https://doi.org/10.1021/jp040677z>
- 675 Liu H, Zou M, Viliam Hakala B, et al (2017) Synthesis, characterization of Cu, N co-doped TiO<sub>2</sub> microspheres with  
676 enhanced photocatalytic activities. *Adv Mater Sci* 2:. <https://doi.org/10.15761/AMS.1000114>
- 677 Liu Z, Teng F (2018a) Understanding the Correlation of Crystal Atoms with Photochemistry Property: Zn<sub>5</sub>(OH)<sub>6</sub>  
678 (CO<sub>3</sub>)<sub>2</sub> vs . ZnCO<sub>3</sub>. *ChemistrySelect* 3:8886–8894. <https://doi.org/10.1002/slct.201801420>
- 679 Liu Z, Teng F (2018b) Understanding the Correlation of Crystal Atoms with Photochemistry Property: Zn<sub>5</sub>(OH)<sub>6</sub>  
680 (CO<sub>3</sub>)<sub>2</sub> vs . ZnCO<sub>3</sub>. *ChemistrySelect* 3:8886–8894. <https://doi.org/10.1002/slct.201801420>
- 681 Mathew S, Ganguly P, Rhatigan S, et al (2018) Cu-Doped TiO<sub>2</sub>: Visible Light Assisted Photocatalytic Antimicrobial  
682 Activity. *Applied Sciences* 8:2067. <https://doi.org/10.3390/app8112067>
- 683 Meribout R, Zuo Y, Khodja AA, et al (2016) Photocatalytic degradation of antiepileptic drug carbamazepine with  
684 bismuth oxychlorides (BiOCl and BiOCl/AgCl composite) in water: Efficiency evaluation and elucidation  
685 degradation pathways. *Journal of Photochemistry and Photobiology A: Chemistry* 328:105–113.  
686 <https://doi.org/10.1016/j.jphotochem.2016.04.024>
- 687 Mittal A, Kaur D, Mittal J (2009) Batch and bulk removal of a triarylmethane dye, Fast Green FCF, from wastewater  
688 by adsorption over waste materials. *Journal of Hazardous Materials* 163:568–577.  
689 <https://doi.org/10.1016/j.jhazmat.2008.07.005>
- 690 Mucklow JC (2000) Martindale: The Complete Drug Reference: Book review. *British Journal of Clinical*  
691 *Pharmacology* 49:613–613. <https://doi.org/10.1046/j.1365-2125.2000.00206.x>
- 692 Nakamura R, Frei H (2006) Visible Light-Driven Water Oxidation by Ir Oxide Clusters Coupled to Single Cr Centers in  
693 Mesoporous Silica. *J Am Chem Soc* 128:10668–10669. <https://doi.org/10.1021/ja0625632>
- 694 Olowoyo JO, Kumar M, Dash T, et al (2018) Self-organized copper impregnation and doping in TiO<sub>2</sub> with enhanced  
695 photocatalytic conversion of H<sub>2</sub>O and CO<sub>2</sub> to fuel. *International Journal of Hydrogen Energy* 43:19468–  
696 19480. <https://doi.org/10.1016/j.ijhydene.2018.08.209>
- 697 Papp J, Shen HS, Kershaw R, et al (1993) Titanium(IV) oxide photocatalysts with palladium. *Chem Mater* 5:284–288.  
698 <https://doi.org/10.1021/cm00027a009>
- 699 Pava-Gómez B, Vargas-Ramírez X, Díaz-Urbe C, et al (2021) Evaluation of copper-doped TiO<sub>2</sub> film supported on  
700 glass and LDPE with the design of a pilot-scale solar photoreactor. *Solar Energy* 220:695–705.  
701 <https://doi.org/10.1016/j.solener.2021.03.071>
- 702 Pérez-Estrada LA, Malato S, Gernjak W, et al (2005) Photo-Fenton Degradation of Diclofenac: Identification of Main  
703 Intermediates and Degradation Pathway. *Environ Sci Technol* 39:8300–8306.  
704 <https://doi.org/10.1021/es050794n>
- 705 Pirillo S, Pedroni V, Rueda E, Luján Ferreira M (2009) Elimination of dyes from aqueous solutions using iron oxides  
706 and chitosan as adsorbents: a comparative study. *Quím Nova* 32:1239–1244.  
707 <https://doi.org/10.1590/S0100-40422009000500030>

- 708 Rafqah S, Sarakha M (2016) Photochemical transformation of flufenamic acid by artificial sunlight in aqueous  
709 solutions. *Journal of Photochemistry and Photobiology A: Chemistry* 316:1–6.  
710 <https://doi.org/10.1016/j.jphotochem.2015.10.003>
- 711 Rafqah S, Seddigi ZS, Ahmed SA, et al (2015) Use of quadrupole time of flight mass spectrometry for the  
712 characterization of transformation products of the antibiotic sulfamethazine upon photocatalysis with Pd-  
713 doped ceria-ZnO nanocomposite: Hydroxylation sites of sulfamethazine. *J Mass Spectrom* 50:298–307.  
714 <https://doi.org/10.1002/jms.3521>
- 715 Rafqah S, Wong-Wah-Chung P, Nelieu S, et al (2006) Phototransformation of triclosan in the presence of TiO<sub>2</sub> in  
716 aqueous suspension: Mechanistic approach. *Applied Catalysis B: Environmental* 66:119–125.  
717 <https://doi.org/10.1016/j.apcatb.2006.03.004>
- 718 Rathod M, Moradeeya PG, Haldar S, Basha S (2018) Nanocellulose/TiO<sub>2</sub> composites: preparation, characterization  
719 and application in the photocatalytic degradation of a potential endocrine disruptor, mefenamic acid, in  
720 aqueous media. *Photochem Photobiol Sci* 17:1301–1309. <https://doi.org/10.1039/C8PP00156A>
- 721 Rueda-Márquez JJ, Moreno-Andrés J, Rey A, et al (2021) Post-treatment of real municipal wastewater effluents by  
722 means of granular activated carbon (GAC) based catalytic processes: A focus on abatement of  
723 pharmaceutically active compounds. *Water Research* 192:116833.  
724 <https://doi.org/10.1016/j.watres.2021.116833>
- 725 [Shao M, Han J, Wei M, et al \(2011\) The synthesis of hierarchical Zn–Ti layered double hydroxide for efficient  
726 visible-light photocatalysis. \*Chemical Engineering Journal\* 168:519–524.  
727 <https://doi.org/10.1016/j.cej.2011.01.016>](#)
- 728 Shen T, Han T, Zhao Q, et al (2022) Efficient removal of mefenamic acid and ibuprofen on organo-Vts with a  
729 quinoline-containing gemini surfactant: Adsorption studies and model calculations. *Chemosphere*  
730 295:133846. <https://doi.org/10.1016/j.chemosphere.2022.133846>
- 731 Shirzadi A, Nezamzadeh-Ejhieh A (2016) Enhanced photocatalytic activity of supported CuO–ZnO semiconductors  
732 towards the photodegradation of mefenamic acid aqueous solution as a semi real sample. *Journal of*  
733 *Molecular Catalysis A: Chemical* 411:222–229. <https://doi.org/10.1016/j.molcata.2015.10.027>
- 734 Sim W-J, Lee J-W, Oh J-E (2010) Occurrence and fate of pharmaceuticals in wastewater treatment plants and rivers  
735 in Korea. *Environmental Pollution* 158:1938–1947. <https://doi.org/10.1016/j.envpol.2009.10.036>
- 736 Soulet B, Tauxe A, Tarradellas J (2002) Analysis of Acidic Drugs in Swiss Wastewaters. *International Journal of*  
737 *Environmental Analytical Chemistry* 82:659–667. <https://doi.org/10.1080/0306731021000075384>
- 738 Sreethawong T, Yoshikawa S (2005) Comparative investigation on photocatalytic hydrogen evolution over Cu-, Pd-,  
739 and Au-loaded mesoporous TiO<sub>2</sub> photocatalysts. *Catalysis Communications* 6:661–668.  
740 <https://doi.org/10.1016/j.catcom.2005.06.004>
- 741 Sui Q, Cao X, Lu S, et al (2015) Occurrence, sources and fate of pharmaceuticals and personal care products in the  
742 groundwater: A review. *Emerging Contaminants* 1:14–24. <https://doi.org/10.1016/j.emcon.2015.07.001>
- 743 Sun L, Wan S, Luo W (2013) Biochars prepared from anaerobic digestion residue, palm bark, and eucalyptus for  
744 adsorption of cationic methylene blue dye: Characterization, equilibrium, and kinetic studies. *Bioresource*  
745 *Technology* 140:406–413. <https://doi.org/10.1016/j.biortech.2013.04.116>
- 746 Tauxe-Wuersch A, De Alencastro LF, Grandjean D, Tarradellas J (2005) Occurrence of several acidic drugs in sewage  
747 treatment plants in Switzerland and risk assessment. *Water Research* 39:1761–1772.  
748 <https://doi.org/10.1016/j.watres.2005.03.003>
- 749 Ternes TA, Meisenheimer M, McDowell D, et al (2002) Removal of Pharmaceuticals during Drinking Water  
750 Treatment. *Environ Sci Technol* 36:3855–3863. <https://doi.org/10.1021/es015757k>

- 751 Tijani JO, Fatoba OO, Madzivire G, Petrik LF (2014) A Review of Combined Advanced Oxidation Technologies for the  
752 Removal of Organic Pollutants from Water. *Water Air Soil Pollut* 225:2102.  
753 <https://doi.org/10.1007/s11270-014-2102-y>
- 754 Turianicová E, Kaňuchová M, Zorkovská A, et al (2016) CO<sub>2</sub> utilization for fast preparation of nanocrystalline  
755 hydrozincite. *Journal of CO<sub>2</sub> Utilization* 16:328–335. <https://doi.org/10.1016/j.jcou.2016.08.007>
- 756 Tzompantzi-Flores C, Castillo-Rodríguez JC, Gómez R, et al (2020) Photocatalytic Evaluation of the  
757 ZrO<sub>2</sub>:Zn<sub>5</sub>(OH)<sub>6</sub>(CO<sub>3</sub>)<sub>2</sub> Composite for the H<sub>2</sub> Production via Water Splitting. *Top Catal* 63:575–585.  
758 <https://doi.org/10.1007/s11244-020-01236-9>
- 759 Tzompantzi-Flores C, Castillo-Rodríguez JC, Gómez R, et al (2019) Synthesis and characterization of ZnZr  
760 composites for the photocatalytic degradation of phenolic molecules: addition effect of ZrO<sub>2</sub> over  
761 hydrozincite Zn<sub>5</sub>(OH)<sub>6</sub>(CO<sub>3</sub>)<sub>2</sub>. *J Chem Technol Biotechnol* 94:3428–3439.  
762 <https://doi.org/10.1002/jctb.5928>
- 763 Vogna D, Marotta R, Napolitano A, et al (2004) Advanced oxidation of the pharmaceutical drug diclofenac with  
764 UV/H<sub>2</sub>O<sub>2</sub> and ozone. *Water Research* 38:414–422. <https://doi.org/10.1016/j.watres.2003.09.028>
- 765 Wang M, Zhao Q, Yang H, et al (2020) Photocatalytic antibacterial properties of copper doped TiO<sub>2</sub> prepared by  
766 high-energy ball milling. *Ceramics International* 46:16716–16724.  
767 <https://doi.org/10.1016/j.ceramint.2020.03.246>
- 768 Wang X-R, Li Y, Tang L-P, et al (2017) Fabrication of Zn-Ti layered double hydroxide by varying cationic ratio of Ti<sup>4+</sup>  
769 and its application as UV absorbent. *Chinese Chemical Letters* 28:394–399.  
770 <https://doi.org/10.1016/j.ccllet.2016.09.002>
- 771 Wei X, Wang Y, Chen J, et al (2020) Adsorption of pharmaceuticals and personal care products by deep eutectic  
772 solvents-regulated magnetic metal-organic framework adsorbents: Performance and mechanism.  
773 *Chemical Engineering Journal* 392:124808. <https://doi.org/10.1016/j.cej.2020.124808>
- 774 Wu C, De Visscher A, Gates ID (2017) Reactions of hydroxyl radicals with benzoic acid and benzoate. *RSC Adv*  
775 7:35776–35785. <https://doi.org/10.1039/C7RA05488B>
- 776 Yagub MT, Sen TK, Afroze S, Ang HM (2014) Dye and its removal from aqueous solution by adsorption: A review.  
777 *Advances in Colloid and Interface Science* 209:172–184. <https://doi.org/10.1016/j.cis.2014.04.002>
- 778 Yan C, Xue D (2006a) Morphosynthesis of Hierarchical Hydrozincite with Tunable Surface Architectures and Hollow  
779 Zinc Oxide. *J Phys Chem B* 110:11076–11080. <https://doi.org/10.1021/jp060357a>
- 780 Yan C, Xue D (2006b) Morphosynthesis of Hierarchical Hydrozincite with Tunable Surface Architectures and Hollow  
781 Zinc Oxide. *J Phys Chem B* 110:11076–11080. <https://doi.org/10.1021/jp060357a>
- 782 Yu Y, Wang J, Li W, et al (2015) Doping mechanism of Zn<sup>2+</sup> ions in Zn-doped TiO<sub>2</sub> prepared by a sol-gel method.  
783 *CrystEngComm* 17:5074–5080. <https://doi.org/10.1039/C5CE00933B>
- 784 Zheng H, Li J, Zhang X, et al (2015) Structural and electronic properties of Cu-doped Zn<sub>5</sub>(OH)<sub>6</sub>(CO<sub>3</sub>)<sub>2</sub> from first  
785 principles. *J Mater Sci* 50:6794–6807. <https://doi.org/10.1007/s10853-015-9237-0>

786